Monthly Notices
of the
ROYAL ASTRONOMICAL SOCIETY

MNRAS **512,** 4639–4659 (2022)
Advance Access publication 2022 February 24

https://doi.org/10.1093/mnras/stac514

Discovery of a bright extended X-ray jet in RGB J1512+020A

G. Migliori [1,2★] A. Siemiginowska,[3] C. C. Cheung,[4] A. Celotti,[5,6,7] M. Giroletti [1] G. Giovannini,[1,2] A. Paggi[8,9,10] and E. Liuzzo[1]

[1]*Istituto di Radioastronomia – INAF, Via P. Gobetti 101, I-40129 Bologna, Italy*
[2]*Dipartimento di Fisica e Astronomia, Università di Bologna, Via Gobetti 93/2, I-40129 Bologna, Italy*
[3]*Center for Astrophysics, Harvard and Smithsonian, 60 Garden St., Cambridge, MA 02138, USA*
[4]*Space Science Division, Naval Research Laboratory, Washington, DC 20375, USA*
[5]*Scuola Internazionale Superiore di Studi Avanzati (SISSA), via Bonomea, I-265-34136 Trieste Italy*
[6]*INAF – Osservatorio Astronomico di Brera, Via E. Bianchi 46, I-23807 Merate, Italy*
[7]*INFN – National Institute for Nuclear Physics, Via Valerio 2, I-34127 Trieste, Italy*
[8]*Dipartimento di Fisica, Università degli Studi di Torino, via Pietro Giuria 1, I-10125 Torino, Italy*
[9]*INAF – Osservatorio Astrofisico di Torino, via Osservatorio 20, I-10025 Pino Torinese, Italy*
[10]*Istituto Nazionale di Fisica Nucleare, Sezione di Torino, via Pietro Giuria 1, I-10125 Turin, Italy*

Accepted 2022 February 15. Received 2022 February 13; in original form 2021 May 5

ABSTRACT

We report the discovery of a bright, extended X-ray jet in the quasar RGB J1512+020A ($z = 0.22$). *Chandra* observations show the X-ray core and 13 arcsec (∼45 kpc projected) extended emission coincident with the radio jet. The jet stands out as one of brightest X-ray jets ($L_X \sim 7 \times 10^{43}$ erg s^{-1}) at low redshift ($z < 0.5$) discovered so far, with remarkably large X-ray to radio luminosity ratios (L_X/L_r up to ∼50). We identified four main components, two unresolved knots and two extended structures, one being the jet brightest feature (JBF). All jet features are also detected in ALMA archival observations. The radio, sub-mm to X-ray spectra of the two knots can be modelled with a single synchrotron component. For the two resolved structures, the ALMA data unveil a turnover of the low-energy continuum at ∼460 GHz. External Comptonization of cosmic microwave background photons can account for the observed X-ray emission if the jet speed remains highly relativistic, with bulk motion $\Gamma_{\rm bulk} > 15$, up to tens of kiloparsec from the core. However, the comparison with the spectral energy distribution of similar X-ray detected jets shows that the alternative hypothesis of synchrotron emission from an additional population of ultra-high-energy electrons is also possible. We report a tentative ($\gtrsim 2\sigma$) optical detection of the JBF in images of the Dark Energy Camera Legacy Survey. If confirmed, the optical emission should be either the low-energy tail of the radiative component responsible for the X-ray emission or a third, separate component.

Key words: radiation mechanisms: non-thermal – galaxies: active – galaxies: jets – X-rays: galaxies.

1 INTRODUCTION

In relativistic jets powered by supermassive black holes (SMBHs), radio to γ-ray emission can be observed in compact, sub-parsec-scale regions to extended, kilo-parsec structures (see Blandford, Meier & Readhead 2019, for a recent review). The observed radio to γ-ray spectral energy distributions (SEDs) show that a significant, often dominant, fraction of the jet radiated power is released in the X-ray to γ-ray band, thus the study of this high-energy component is central to our understanding of jets.

X-ray emission is detected up to hundreds of kiloparsecs from the SMBH, in jets, hotspots, and lobes (Sambruna et al. 2004; Hogan et al. 2011; Massaro, Harris & Cheung 2011; Marshall et al. 2018; Massaro et al. 2018). In jets of low-power Fanaroff Riley type I radio galaxies (FR I, Fanaroff & Riley 1974), characterized by a surface brightness decreasing with the increasing distance from the core and wide opening angles, the synchrotron origin of the X-ray emission appears well-established. The process responsible for the X-ray radiation of powerful FR II jets, which are typically collimated on kpc-scales and edge-brightened, is instead still a puzzle (Harris & Krawczynski 2006; Worrall 2009). Inverse Compton (IC) off the radio-to-optical synchrotron photons produced in the jet (synchrotron self-Compton, SSC) and off cosmic microwave background photons (IC/CMB; Tavecchio et al. 2000; Celotti, Ghisellini & Chiaberge 2001) are naturally expected. The IC/CMB component should be more relevant in jets of sources at high redshift because of the increase of the CMB energy density (Schwartz 2002; Mocz, Fabian & Blundell 2011; Fabian et al. 2014, and references therein). Indeed, this was the scenario proposed for the X-ray emission of a number of high-redshift quasars (Siemiginowska et al. 2003; Cheung, Stawarz & Siemiginowska 2006; Erlund et al. 2006; Cheung et al. 2012; Simionescu et al. 2016; Medvedev et al. 2020; Schwartz et al. 2020; Worrall et al. 2020). On the other hand, tests of the IC/CMB model predictions based on X-ray surveys of jetted quasars have not given univocal results (see Hogan et al. 2011; McKeough et al. 2016; Marshall et al. 2018; Zhu et al. 2019, and references therein). One limitation to perform statistically meaningful tests is represented by the relatively low number of resolved X-ray jets, in particular at high redshift.

★ E-mail: giulia.migliori@inaf.it

In several jets, however, both processes, SSC and IC/CMB, require extreme values of the physical parameters (e.g. large particle to magnetic field energy density ratios, deprojected linear length, jet power, bulk-flow Lorentz factors), in order to account for the observed X-ray luminosities. Alternatively, synchrotron emission from a second population of electrons, which should be accelerated to TeV energies, has been proposed (Harris & Krawczynski 2002; Stawarz & Ostrowski 2002; Atoyan & Dermer 2004; Kataoka & Stawarz 2005). A further possibility, although relatively less explored for kiloparsec jets thus far, is represented by hadronic emission models (see e.g. Aharonian 2002; Kusunose & Takahara 2017; Petropoulou, Vasilopoulos & Giannios 2017).

Each scenario has important implications on key aspects of jet physics, concerning the particle acceleration mechanism, the jet dynamical structure, and the amount of energy carried by the jet, hence also on its impact on the surrounding environment. An IC/CMB origin of the X-ray emission implies relativistic jet velocity on kiloparsec scales and low energy dissipation. On the other hand, the scenario of a second synchrotron component requires an efficient particle acceleration mechanism active far from the jet launching site and could indicate a stratified velocity structure of the jet plasma (Georganopoulos & Kazanas 2003; Tavecchio 2020).

Currently, there are about 150 X-ray detected jets (Massaro et al. 2011; Marshall et al. 2018). In order to discriminate between the different scenarios, multiwavelength and deep X-ray observations are needed in order to perform detailed, spatially resolved studies (see e.g. Cygnus A, Pictor A, 3C 111, 3C 273, PKS 1127−145; Marshall et al. 2001; Jester et al. 2006; Siemiginowska et al. 2007; Marshall et al. 2010; Clautice et al. 2016; de Vries et al. 2018). In the case of the X-ray jet of 3C 273, infrared (IR) to ultraviolet (UV) data have established a common origin of the bulk of the optical and X-ray flux (Jester et al. 2006; Uchiyama et al. 2006). A test of the IC/CMB scenario based on γ-ray observations has been proposed by Georganopoulos et al. (2006) and applied to a number of quasars' X-ray jets using *Fermi* data (see Meyer & Georganopoulos 2014; Meyer et al. 2015; Breiding et al. 2017, for 3C 273, PKS 0637-752, and a mini-sample, respectively), giving evidence of a possible inconsistency between theoretical predictions and observations.

Here, we report the discovery of X-ray emission associated with the radio jet of the quasar RGB J1512+020A (PKS 1509+022; Laurent-Muehleisen et al. 1997) located at redshift, $z = 0.220$ (Wills & Wills 1976; Hewett & Wild 2010), and we present for the first time the X-ray jet morphology revealed by the *Chandra* observations. Our analysis include radio maps from archival high-resolution Very Large Array (VLA) observations, data taken by the Atacama Millimeter/sub-millimeter Array (ALMA) and optical images from public surveys. In this paper, we focus on the multiwavelength properties of the kiloparsec jet. A detailed study and modelling of the quasar core emission is the subject of a forthcoming paper. Throughout, we assume a ΛCDM cosmology with $H_0 = 70$ km s^{-1} Mpc^{-1}, $\Omega_m = 0.27$, and $\Omega_\Lambda = 0.73$, corresponding to an angular scale of 1 arcsec = 3.5 kpc at the redshift of RGB J1512+020A.

1.1 RGB J1512+020A

RGB J1512+020A (hereafter J1512+02) was detected in X-rays as part of the *ROSAT* All-Sky Survey (RASS; Voges et al. 1999). In RASS, the source is unresolved and has a 0.1–2.4 keV flux of $(0.955 \pm 0.268) \times 10^{-12}$ erg cm^{-2} s^{-1} (Siebert et al. 1998). J1512+02 is among the low-redshift, flat-spectrum radio quasars in the RASS/Green Bank (RGB; Laurent-Muehleisen et al. 1997) sample which are characterized by red optical spectra and relatively low soft X-ray luminosities. Dust absorption has been discussed as a possible explanation for these features (Webster et al. 1995; Siebert et al. 1998).

In the literature, its optical classification is not univocally defined. In the Sloan Digital Sky Survey (SDSS) seven data release quasar catalogue (Shen et al. 2011), it is classified as a quasar based on an absolute magnitude M_i brighter than −22 and the detection of the broad H_α emission line (and with an estimated line luminosity of 6.6×10^{41} erg s^{-1}). However, the H_β line is not present in the spectrum acquired by Baldwin, Wampler & Gaskell (1989) and is only marginally detected in the SDSS spectrum (6.5×10^{41} erg s^{-1}; Shen et al. 2011), while the UV continuum of the core appears unusually weak for a typical quasar (Wills & Wills 1976; Baldwin et al. 1989). For this reason, the source was at times classified as a Seyfert I galaxy (Wills & Wills 1976).

The source is listed in several radio survey catalogues (Parkes radio survey, Texas Survey, and Green Bank 5 GHz survey with a 408 MHz flux of 2.38 Jy) with a measured flat spectrum between 2.7 and 5 GHz, $\alpha_{2.7}^{5.0} = 0.40$ (flux density $S_\nu \propto \nu^{-\alpha}$; Wright & Otrupcek 1990) and a double-lobed radio morphology at 5 arcsec resolution (de Vries et al. 2006). Its core to lobe flux ratio, the so-called radio core dominance,[1] $R = 0.34$, is intermediate between radio galaxies ($<R> = 0.019$; Laurent-Muehleisen et al. 1997) and core-dominated sources ($R > 1$).

In the Fourth catalogue of *Fermi* LAT sources (4FGL; Abdollahi et al. 2020), J1512+02 is associated with the γ-ray source 4FGL J1512.2+0202. When modelled with a single power law, its γ-ray spectrum has a photon index $\Gamma_\gamma = 2.2$ and a 1–100 GeV flux of $(2.0 \pm 0.2) \times 10^{-9}$ phot cm^{-2} s^{-1}. Indeed, except for the class of γ-ray emitting misaligned active galactic nuclei (MAGN; Abdo et al. 2010; Ajello et al. 2020), the detection of γ-ray emission is more often associated with jets aligned close to the line of sight (collectively referred to as blazar sources).

2 CHANDRA OBSERVATION

J1512+02 was observed for the first time with the ACIS-S camera onboard the *Chandra* X-ray Observatory for ∼3 ksec on 2005 March 27 (ObsID 5671, PI: S. Laurent-Muehleisen). The discovery of extended X-ray emission, while inspecting this archival data set, led us to request a second, ∼27 ksec long observation, which was performed on 2017 June 5 (ObsID 19563, PI: Migliori).

In the first observation, the target was placed 30 arcsec from the default aim-point position on the ACIS-S backside illuminated S3 chip. The data were collected in the faint mode, using a 1/8 subarray configuration (frame time of 0.4 s) that reduces pileup effects in the observations of bright sources. The same parameters were set for the second observation with the only differences that the core of the source was at the default aim-point and a very faint mode was used.

The X-ray data analysis was conducted with the CIAO 4.12 software (Fruscione et al. 2006) using the calibration file version CALDB v. 4.9.3. We ran the `chandra_repro` reprocessing script that performs all the analysis steps. After standard filtering, the effective exposure time was 2.89 ksec for the first observation and 27.04 ksec for the second one.

[1]Here, we adopt the definition in Laurent-Muehleisen et al. (1997) with $R = F_{core}/(F_{tot} - F_{core})$ with F_{core} and F_{tot} being the 5 GHz flux of the core and the total one, respectively. R is an indicator of the angle between the radio jet axis and the observer line of sight. Typically, aligned and beamed sources have $R > 1$ and are defined core-dominated.

For imaging purposes, we merged the two observations. The 0.3–8 keV image in Fig. 1 (lower panels) clearly shows an unresolved bright source, identified with the quasar X-ray core, and extended X-ray emission in the southern direction, coincident with the position of the radio jet (Section 3 and Fig. 1, upper panels).

The 0.3–8 keV count rates of the core, measured in a circular region with radius 1.5 arcsec, are 0.2 counts s^{-1} and 0.1 counts s^{-1} in the first and last observation, respectively, which give a <3 per cent maximum pileup fraction, as estimated by PIMMS.

The net counts of the core and of the jet resolved features in the soft (0.3–2.5 keV) and hard (2.5–8 keV) X-ray bands were taken from circular regions with radii of 1.5 arcsec (core), 0.9 arcsec (first knot, knot1), 1 arcsec (second knot, knot2), 2.1 arcsec (jet brighest feature, JBF), and 2.9 arcsec (jet termination, see Fig. 2). The same regions were used to extract the X-ray spectra. Two large off-source regions were selected to evaluate the background. In the 2017 observation, to account for contamination of the emission of the first knot by the core, the background spectrum was extracted from a sector region centred on the core and at the same distance as the first knot (the inner and outer radii are 1.5 and 3 arcsec, respectively).

3 RADIO OBSERVATIONS

We analysed archival radio observations of J1512+02 from NRAO[2] VLA programmes AL152 (PI: G. Langston) and S60607 (PI: S. Laurent-Muehleisen). These consisted of snapshot scans obtained on 1987 July 23 and 2004 December 27, respectively, in the highest resolution A-array. Each observing run obtained data in up to three bands, producing maps at ∼1 arcsec resolution and better. All observations used two 50 MHz wide intermediate frequency bands, with centre frequencies of 1.565 GHz (500 s exposure) and 4.86 GHz (380 s) for the AL152 observations and 1.425 GHz, 4.86 GHz, and 8.46 GHz (175, 365, and 605 s, respectively) in programme S60607.

When available, the basic calibrated (u, v) data were downloaded from the NRAO VLA Archive Survey;[3] else, we downloaded the raw data from the NRAO archive and calibrated the data in `AIPS` using standard procedures. Self-calibration and imaging (using `CLEAN`) were performed using `DIFMAP` (Shepherd, Pearson & Taylor 1994). The calibrated L-band (u, v) data from the two programmes were combined in AIPS using DBCON and successfully produced an improved map with respect to the individual data sets with an effective frequency of 1.50 GHz. The 1.50 GHz map was reconvolved with a circular 1.3 arcsec beam (geometric mean of the uniformly weighted beam 1.2 arcsec × 1.4 arcsec).

Similarly, combining the 4.86 GHz data from the two programmes, we did not find an appreciable improvement in the resultant map, thus we only utilized the map from the modestly deeper AL152 observation (0.45 arcsec beam; natural weighting). The 8.46 GHz map has the highest resolution (0.2 arcsec beam; natural weighting), but because of the lack of good (u, v) coverage, particularly at short spacings, the image is missing much of the diffuse emission visible at the lower frequencies, and is likely underestimating the fluxes of the faintest features.

Because of the different angular resolutions of the VLA maps, and their varying quality, we adopted different procedures to measure the radio fluxes and spectra from different emitting components (see Table 1). For the compact, unresolved features in the jet, we used modelfit in `DIFMAP` to fit elliptical Gaussians in the (u, v) plane. For extended, resolved regions, we used ds9 to measure the fluxes in the *Chandra* defined extraction apertures. For sources with simple structures, the absolute uncertainties in the VLA flux calibration can be as small as 1 − 2 per cent (Ulvestad, Perley & Taylor 2007). Due to additional uncertainties induced by the imaging and self-calibration of the complex structures observed in our case, for all the extended jet features we assumed 10 per cent uncertainties in the 4.86 GHz fluxes, and slightly larger 15 per cent errors in the other bands due to complications arising from measurements at lower resolution (1.57 GHz) and sparsely sampled data (8.46 GHz). The core emission is well-defined in the maps and we quote the simultaneous measurements from the 2004 December data with 5 per cent uncertainties in all bands (i.e. slightly larger than the absolute uncertainties). The extended features have spectral indices consistent with $\alpha \sim 0.8$, with the brightest component in the jet characterized by a noticeably harder spectrum ($\alpha \sim 0.5$).

The source was also observed as part of the FIRST VLA survey (Becker, White & Helfand 1995) and we retrieved the map at 1.435 GHz taken in B configuration, with a beam full width at half-maximum (FWHM) of 5.4 arcsec (de Vries et al. 2006).

4 RADIO AND X-RAY MORPHOLOGY

The VLA maps reveal the extended radio structure of J1512+02. A double-lobed morphology is visible in the FIRST map (Fig. 1, upper left-hand panel). At higher angular resolution (≲1 arcsec), the structure appears one-sided with a ∼13 arcsec-long southern jet. The emission from the northern lobe is marginally detected only in the 1.4 GHz map (Fig. 1, upper left-hand panel) and we do not detect any counter-jet, connecting the core to the northern lobe (∼21 arcsec from the core).

The radio image at 4.86 GHz (Fig. 1, upper central panel) shows the unresolved core and the knotty structure of the southern jet. The first knot (knot1), which is unresolved at all radio frequencies, is located at ∼2.2 arcsec from the core at a position angle $PA = 163°$, with an upper limit to the Gaussian FWHM of 0.1 arcsec (corresponding to a diameter of 350 pc) in the 8.46 GHz data. In the highest resolution 8.46 GHz map, the jet extends straight through a 4.5 arcsec distant, unresolved knot (knot2) until a feature at 7 arcsec from the core. The latter appears resolved in the 8.46 GHz map, with a compact component embedded in an extended structure, although the analysis is complicated by the presence of the diffuse radio emission. Fitting of the 8.46 GHz peak with an elliptical Gaussian gives a flux of 17.8 mJy and a size of ∼250 mas × 110 mas. The classification of this feature as a knot or an hotspot is not straightforward. On one side, its compactness is comparable to the radio hotspots in other quasars (Bridle et al. 1994). The deflection of the jet, which could be caused by the jet impacting against the ambient medium, supports this interpretation. In extragalactic jets, abrupt bendings as that observed in J1512+02 are rather common and radio quasars with this structure and a recessed hotspot are dubbed 'dogleg' quasars (see Stocke, Burns & Christiansen 1985). An example is the quasar 3C 275.1, whose hotspot is detected in the radio, optical, and X-ray bands (Crawford & Fabian 2003; Cheung, Wardle & Chen 2005). On the other hand, one can also consider it as a knot, embedded in diffuse radio emission which is visible in the 4.86 GHz map. Indeed, the distinction between knots and hotspots is not uniquely defined (see Hardcastle 2008, for a discussion). In view of this ambiguity, we simply dub this component as jet

[2]The National Radio Astronomy Observatory is a facility of the National Science Foundation operated under cooperative agreement by Associated Universities, Inc.
[3]http://archive.nrao.edu/nvas/

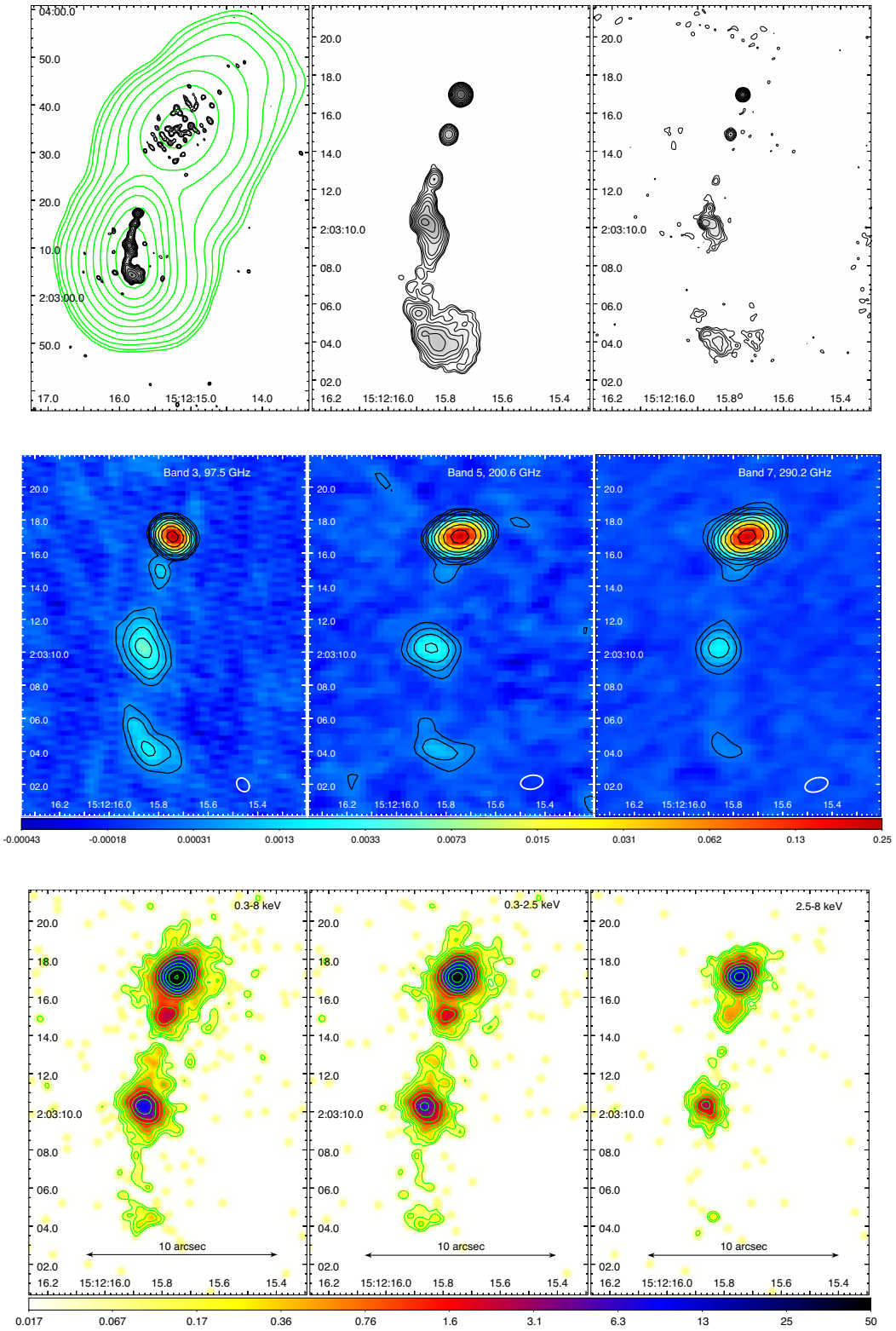

Figure 1. Upper panels: VLA radio maps at 1.5 GHz (left-hand panel), 4.9 GHz (centre), and 8.4 GHz (right-hand panel). The green thick contours in the left-hand panel show the low-resolution radio map at 1.4 GHz from the FIRST survey. Contours are in logarithmic scale and start at 3 × rms. Middle panels: ALMA images in band 3 (left-hand panel, obsID Xc02418_X78c9 in Table 3), band 5 (centre, obsID Xda845c_X15e5b in Table 3) and band 7 (right-hand panel, obsID Xce3de5_Xbec in Table 3). Contours are in logarithmic scale and start at 3 × rms. Lower panels: merged ACIS-S image of the two *Chandra* observations: broad-band (left-hand panel), soft band (centre), and hard band (right-hand panel). The pixel size is set to one quarter of the original ACIS pixel (0.123 arcsec per pix), the colour scale is logarithmic. The image was smoothed using a Gaussian function with $\sigma = 1.5$. Contours start at 5 × rms.

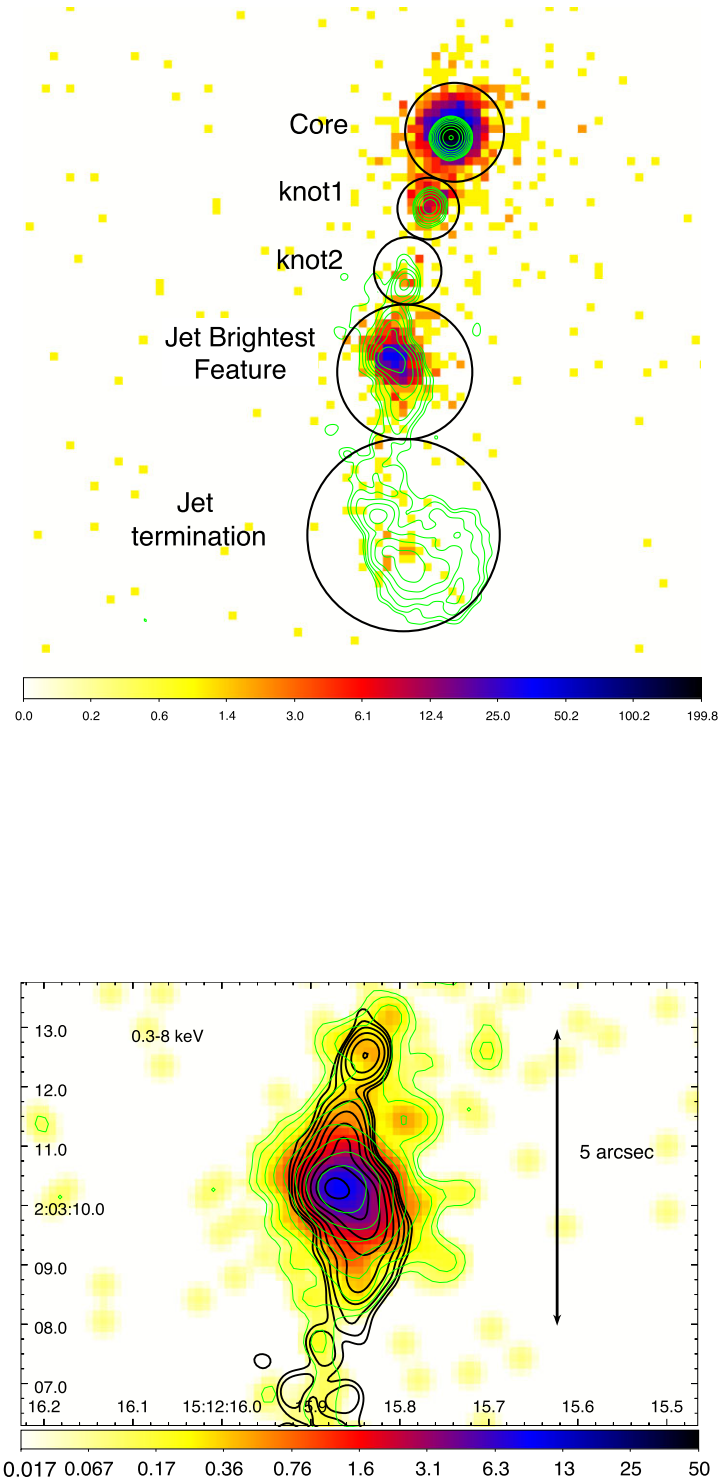

Figure 2. Upper panel: merged *Chandra* image with 4.9 GHz radio contours. The pixel size is set to one quarter of the original ACIS pixel (0.123 arcsec per pix), the colour scale is logarithmic. The black circles are the X-ray extraction regions of the counts and spectra of each feature. Lower panel: close-up view of the knot2 and JBF. Thick black contours are the radio contours at 4.9 GHz, thin green contours are the X-ray ones.

brightest feature (JBF) and we will further discuss its nature in Section 8.1. The radio jet bends before its termination, where the opening angle of the flow increases forming a structure of about ≈2.5 arcsec × 1.5 arcsec size at 4.86 GHz. The extended terminal component presents a radio peak of 10.4 mJy beam^{-1} at 4.86 GHz (jet termination).

The *Chandra* observations show a bright X-ray jet (see Fig. 1). Together with the X-ray core (coincident with the position of the radio

Table 1. RGBJ1512+020A core and jet components.

Component (1)	Position (arcsec kpc^{-1}) (2)	$F_{1.50\,\mathrm{GHz}}$ (3)	$F_{4.86\,\mathrm{GHz}}$ (4)	$F_{8.46\,\mathrm{GHz}}$ (5)	α_{r} (6)
core	–/–	64.3 ± 3.2	178.2 ± 8.9	311.7 ± 15.6	−0.90 ± 0.03
knot1	2.2/7.7	30.6 ± 4.6	11.0 ± 1.1	9.4 ± 1.4	0.76 ± 0.14
knot2	4.7/16.5	14.9 ± 2.2	5.1 ± 0.5	2.2 ± 0.3	0.95 ± 0.16
Jet brightest feature (c)[a]	7.0/24.5	–	23.1 ± 2.3	17.8 ± 2.7	0.47 ± 0.33
Jet brightest feature (ext.)[b]	7.4/25.9	185.9 ± 27.9	99.2 ± 9.9	78.6 ± 11.8	0.52 ± 0.13
Jet termination[c]	13/45.5	232.5 ± 34.9	107.3 ± 10.7	56.1 ± 8.4	0.82 ± 0.11

Notes. Columns: (1) Core and jet component labels: the definitions refer to the features visible in the 4.9 GHz radio maps (see Figs 1 and 2); (2) distance from the core in arcsec and projected distance in kpc; (3) radio flux at 1.50 GHz in mJy (the core flux measurement is at 1.425 GHz); (4) radio flux at 4.86 GHz in mJy; (5) radio flux at 8.46 GHz in mJy; (6) radio spectral indices calculated from all three radio flux densities, with the exception of the following cases. The 8.46 GHz measurement for knot2 likely underestimates its flux so it was omitted in the fit. Also, the compact region embedded in JBF is not sufficiently resolved at 1.50 GHz, so no flux is quoted.
[a]&[b]– compact and extended region of JBF, respectively. The compact region is resolved only in the radio band (see section 4); [c]– the position is taken from the *Chandra* 0.5–8 keV image;

core), the brightest features of the southern radio jet shine also in X-rays at ∼2 arcsec (knot1) and ∼7 arcsec (JBF) from the core. The X-ray emission of the first knot is unresolved. The JBF is the most prominent component also in X-rays. An outer (∼13 arcsec from the core) faint X-ray component is coincident with the last radio peak of the jet termination. The X-ray counts of this feature are spatially distributed within a radius of 1.4 arcsec, and it is unclear whether or not the X-ray emission is extended. In the 0.3–8 keV image (Fig. 1), diffuse X-ray emission is significantly detected until the jet termination. The radio and X-ray flux measurements of the main jet features are reported in Tables 1 and 2.

Fig. 1 shows the X-ray images in the full (0.3–8 keV), soft (0.3–2.5 keV), and hard (2.5–8 keV) bands, and the net (background-subtracted) counts in the three bands for each region are reported in Table 2. In the hard X-rays, the central core, knot1, and JBF are clearly visible, while the bridge of diffuse emission and the jet termination are almost completely suppressed. The extension of the X-ray emission of the JBF along the orthogonal direction to the jet axis is mostly pronounced in the soft band, whereas the 2.5–8 keV counts are distributed within a region of $\lesssim$2 arcsec width.

We investigated the significance of the extended X-ray emission in the JBF by analysing its surface brightness. We ran 50 simulations of the PSF at the location of the JBF using the *Chandra* Ray Tracer (ChaRT) and projected it on to the detector plane with MARX (v 5.3.3). The brightness profile of the observed emission, centred on the X-ray peak of the JBF, was modelled with a PSF model and a constant component to account for the background contamination. Freezing the constant component to the background level measured in a region free from sources, the best-fitting model leaves large residuals at $\gtrsim$0.9 arcsec radius (Fig. 3). If left free to vary, the level of the constant emission exceeds by more than a factor ∼8 the average background and still leaves residual emission at ∼1.0 arcsec radius. The fit improves if we include in the model a component that accounts for the extended emission (Fig. 3), such as a polynomial function or a standard β model (King 1962), with a 1σ lower limit to the β parameter of 0.63. The result is also confirmed by comparing the brightness profile of the JBF with the core emission, assumed to be point-like. For this test, we extracted the profile of the JBF in the 0.3–8, 0.3–2.5, and 2.5–8 keV energy band from a rectangular region, 3 arcsec wide, oriented along the direction orthogonal to the jet main axis (north-east to south-west direction, see Fig. 4). A box with the same dimensions was used for the core profile, which was then rescaled to match the peak of the JBF. The X-ray image was binned to 1/8 of the native pixel size and smoothed with a Gaussian function with $\sigma = 1.5$. In Fig. 4, there is evidence of an excess with respect to the profile of a point-source: the peak of the 0.3–8 keV emission is located to the north-east, aligned with the jet main axis, while the excess appears to extend towards the south-west direction. Next, we analysed the distribution of the soft versus hard X-ray emission (Fig. 4). The profile of the emission in the two bands appears qualitatively different: the hard-band profile is skewed to the north-east side, while the soft emission presents a broader, more symmetric profile.

5 X-RAY SPECTRAL PROPERTIES

Analysis of the X-ray spectra of the core and of the main jet features was performed with Sherpa (version 4.10.1; Freeman, Doe & Siemiginowska 2001). We simultaneously fitted the source spectra of the two epochs and their background spectra. We also looked for spectral variability between the two epochs by separately fitting the 2005 and 2017 data of each feature. Again, the source spectra were simultaneously fitted with their background spectra. Note however that the background contamination in the first, short observation is negligible.

We employed the Cash statistic with the simplex-neldermead method. For the core, which has a large number of counts, we found consistent results applying the χ^2 statistics to model the background-subtracted spectra, grouped so that each energy bin had at least 20 counts. Errors were calculated at 1-σ confidence level for one parameter of interest.

The baseline model adopted initially for all features was a red-shifted, absorbed power-law function. The absorption parameter was initially left free to vary and then fixed to the Galactic value ($N_{\mathrm{H,\,Gal}} = 3.94 \times 10^{20}$ cm^{-2}; Dickey & Lockman 1990) as the analysis did not indicate larger values. A power-law model was adopted to reproduce the background emission. The best-fitting spectral parameters and X-ray fluxes are reported in Table 2.

5.1 Core

A simple power law, corrected for Galactic absorption, provides a good description of the data. The best-fitting photon index of the simultaneous fit of the 2005 and 2017 spectra is $\Gamma_X = 1.53 \pm 0.02$. The unabsorbed 0.5–10 keV flux is $(1.76 \pm 0.06) \times 10^{-12}$ erg cm^{-2} s^{-1}. The photon index and flux of the core are in broad agreement with those measured by *ROSAT*, $\Gamma_X = 1.9^{+0.4}_{-0.6}$ and $(1.0 \pm 0.3) \times$

Table 2. X-ray counts and best-fitting spectral parameters.

Year	0.3–2.5 keV Net counts	2.5–8 keV Net counts	Γ_X	F_X $\times 10^{-13}$ erg cm^{-2} s^{-1}
(1)	(2)	(3)	(4)	(5)
		Core		
2005+2017	2556 ± 51	1052 ± 32	1.53 ± 0.02	18.0 ± 0.6
2005	487 ± 22	96 ± 10	1.73 ± 0.07	18 ± 2
2017	2061 ± 45	951 ± 31	$1.48^{+0.06}_{-0.02}$	18 ± 1
		Knot1		
2005+2017	131 ± 11	37 ± 6	1.6 ± 0.1	1.2 ± 0.2
2005	19 ± 4	5 ± 2	1.4 ± 0.3	1.8 ± 0.7
2017	113 ± 11	31 ± 6	1.7 ± 0.2	1.2 ± 0.2
		Knot2(*)		
2005+2017	28 ± 5	7 ± 3	1.8 ± 0.6	0.19 ± 0.04
2005	5 ± 2	0	–	–
2017	23 ± 5	7 ± 3	1.8 ± 0.6	0.19 ± 0.04
		Jet brightest feature		
2005+2017	528 ± 23	190 ± 14	1.68 ± 0.06	3.2 ± 0.3
2005	83 ± 9	19 ± 4	1.7 ± 0.3	3.2 ± 0.6
2017	447 ± 21	171 ± 13	1.69 ± 0.08	3.2 ± 0.3
		Jet termination(*)		
2005+2017	42 ± 7	12 ± 4	2.1 ± 0.3	0.19 ± 0.05
2005	5 ± 2	1 ± 1	–	–
2017	37 ± 6	11 ± 3	2.1 ± 0.3	0.19 ± 0.05

Notes. Columns: (1) X-ray counts and spectral parameters for the two *Chandra* observations considered together and separately; (2) background subtracted counts between 0.5 and 2.5 keV; (3) background subtracted counts between 2.5 and 8 keV; (4) X-ray best-fitting photon index assuming an absorbed power-law model with the column density fixed to the Galactic value; (5) 0.5–10 keV unabsorbed flux. Uncertainties are quoted at 68 per cent. (*): due to low counts, spectral fitting has not been performed for the 2005 observation.

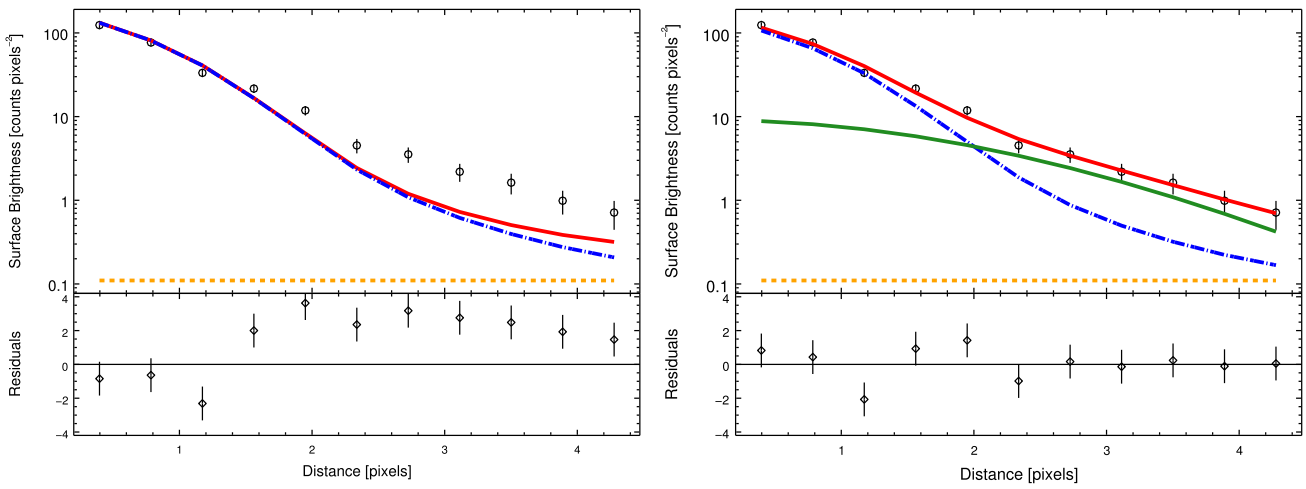

Figure 3. X-ray surface brightness profile of the JBF. Left-hand panel: the best-fitting model (thick solid red curve), which includes the Chandra PSF profile (blue dotted-dashed curves) and a constant background (orange dotted lines), leaves large residuals (lower panel). Right-hand panel: the fit improves when a standard beta model with $\beta > 0.63$ (green short-dotted curve) is included.

10^{-12} erg cm^{-2} s^{-1} in the 0.1–2.4 keV energy range (Siebert et al. 1998), and by the *Swift* X-ray Telescope (XRT), $\Gamma_X = 1.5 \pm 0.2$ and $(1.9 \pm 0.3) \times 10^{-12}$ erg cm^{-2} s^{-1} in the 0.5–10 keV band (observations performed from 2014 June to July; Migliori et al., in preparation), once we take into account the different energy range and spatial resolutions of the three observatories. More complex spectral models, including e.g. a break in the X-ray power law or a thermal component which would account for emission from circumnuclear hot gas, did not significantly improve the fit.

The fit results are driven by the high signal-to-noise spectrum in the deeper 2017 observation. Separately fitting each spectrum shows that the photon index is significantly harder in 2017 ($\Gamma_X = 1.48^{+0.06}_{-0.02}$) than in 2005 ($\Gamma_X = 1.73 \pm 0.07$). Remarkably, the spectral shape change is not associated with a significant change of the 0.5–10 keV flux. We first investigated whether the variation of slope was intrinsic to the source or due to instrumental effects. The estimated fraction of pile up is low ($\lesssim$3 per cent), hence it is not expected to significantly impact the Γ_X value. The ACIS effective area below 2 keV has declined in the period between the two observations,[4] thus affecting the detection of soft X-ray photons, however a calibration model to

[4]https://cxc.cfa.harvard.edu/proposer/POG

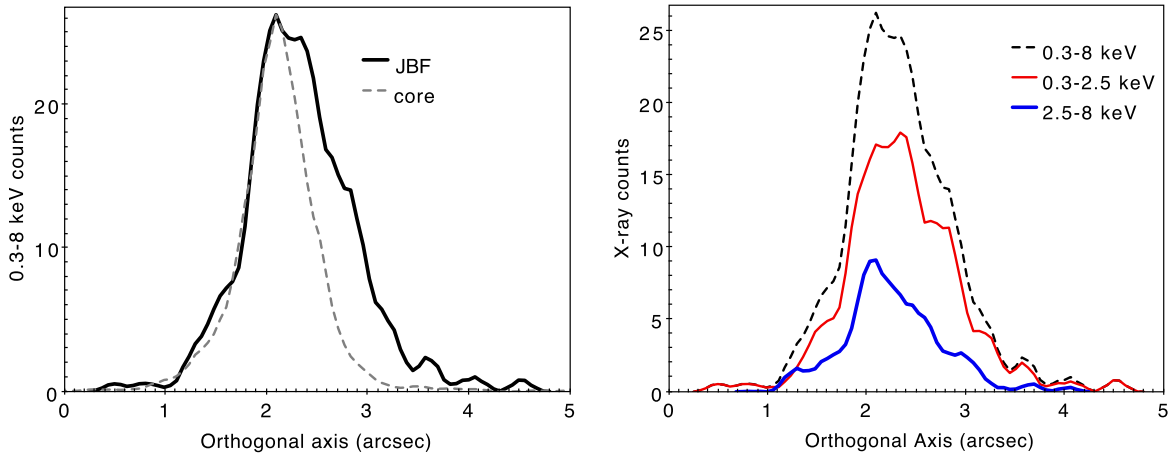

Figure 4. X-ray brightness profiles of the JBF. The profiles were calculated within ds9 using a `projection` region of 3 arcsec width oriented with an angle of 148° (calculated from the North axis, counterclock direction). Left-hand panel: the 0.3–8 keV profile of the JBF is compared with the renormalized core profile, which represents the profile of an unresolved source. The peak of the JBF is to the north-east direction, while excess above the point-like emission is visible to the south-west. Right-hand panel: distribution of the integrated 0.3–8 keV, soft (0.3–2.5 keV), and hard (2.5–8 keV) counts along the profile.

account for this effect is included in the CALDB. Furthermore, the same trend is not found for the other two brightest features, the first knot and the JBF, disfavoring an instrumental origin of the spectral change of the core. Next, we verified whether the variation is due to spectral components or parameters other than the power-law photon index. We tested for an intrinsic absorber to the spectral model of the 2017 data set. If left free to vary, we obtained $N_{\rm H_z} \leq 8 \times 10^{20}$ cm^{-2}, thus indicating only a marginal excess with respect to the Galactic value. Conversely, fixing the photon index to the 2005 value requires $N_{\rm H_z} = (1.7 \pm 0.4) \times 10^{21}$ cm^{-2}. There is not a strong evidence of thermal emission, whose parameters are loosely constrained only in the fit of the 2017 spectrum (kT $= 1.0^{+3.0}_{-0.7}$ and a 0.5–10 keV flux $\sim 4 \times 10^{-14}$ erg cm^{-2} s^{-1}). If we include the thermal component in the spectral model of the 2005 data set, fixing the parameters to the 2017 values, the photon index hardens ($\Gamma_X = 1.6 \pm 0.1$). In conclusion, while a transient event of mild obscuration or emission from hot plasma are still possible explanations of the spectral change between the two epochs, the spectral analysis favours a change of the intrinsic photon index value, thus a variation of the non-thermal component.

The hard X-ray photon index is broadly consistent with values measured in the X-ray spectra of luminous blazars detected in γ-rays ($\Gamma_{\rm X} \sim 1.6$; Abdo et al. 2010; Ghisellini et al. 2010; Giommi et al. 2012; Marshall et al. 2018), where the non-thermal emission produced in a compact, highly relativistic region (the so-called blazar region) is the dominant contribution. Indeed, Sbarrato et al. (2012) have shown that the blazar broad-band emission of J1512+02 can be described by a synchrotron-IC leptonic model. Modelling of the SED of the core will be presented in a dedicated paper.

5.2 X-ray jet

Spectral modelling of the X-ray emission of the jet components identified in the radio maps was performed for all features but the second radio knot, which has a low number of counts ($\lesssim$25 counts) in both observations. We used PIMMS to convert the count rate of the second knot to the unabsorbed monochromatic (1 keV) flux ($\nu F_{\nu,\,1{\rm keV}}$ $\sim 3 \times 10^{-15}$ erg cm^{-2} s^{-1}).

First knot (knot 1 region) – By simultaneously fitting the 2005 and 2017 data sets with a power-law model we obtained the best-fitting photon index $\Gamma_{\rm X} = 1.6 \pm 0.1$ and a 0.5–10 keV flux of $(1.2 \pm 0.2) \times 10^{-13}$ erg cm^{-2} s^{-1}. These values are in agreement within the uncertainties with those obtained by separately fitting the two spectra.

Jet brightest feature (JBF) – The best-fitting photon index is 1.68 ± 0.06. The same value, although with larger uncertainties, is found in the individual analysis of the data sets. We investigated the possibility that the extended emission revealed by the morphological analysis is due to a different spectral component. To this aim, we tested a broken power-law model and, alternatively, adding a thermal component to the power-law model. In both cases, the fit did not improve and the models' parameters were not constrained by the fit. We conclude that the bulk of the emission is related to a single non-thermal component.

Jet termination – The 2017 observation improved our view of the jet termination with respect to the first snapshopt, for which only a marginal detection could be obtained (7 ± 3 net counts). About 46 net counts are retrieved from this region in the 0.3–8 keV energy range, allowing for a basic modelling of the emission. The best fit $\Gamma_{\rm X}$ is 2.1 ± 0.3, remarkably softer, although with large uncertainties, than the values measured for the other jet features. The unabsorbed 0.5–10 keV flux is $(1.9 \pm 0.5) \times 10^{-14}$ erg cm^{-2} s^{-1}. The data can be equally described by a thermal emission model with a best-fitting temperature $kT = 4^{+2}_{-1}$ keV. While emission from gas shock-heated by the expanding jet (or lobe) is possible, the temperatures reported in these cases are typically lower ($\lesssim$1 keV; see Cen A, 4C 29.30; Croston et al. 2009; Siemiginowska et al. 2012), though with notable exceptions as for the hot ($\sim$3.5 keV) gas shell in the south-western lobe of Cen A (Kraft et al. 2007).

6 MILLIMETRE TO OPTICAL ARCHIVAL DATA

6.1 ALMA

J1512+02 has been observed at sub-/millimetre wavelengths because the source is a phase calibrator in observations by ALMA. Our target was pointed several times at different epochs, with the

observing band/frequency and configurations determined by the scientific goals of each programme. Calibrated images of J1512+02 were produced and kindly provided by the team of the ALMACAL project.[5] ALMACAL makes use of the fields around the calibrators of projects stored in the ALMA Science Archive to carry out a wide and deep sub-/millimetre survey (Oteo et al. 2016). The observations used for our analysis cover band 3 through 8 (97–466 GHz central frequency) and have a nominal resolution ranging from sub-arcsecond to a few arcseconds. The list of observations is presented in Table 3 and the details of the calibration and imaging process are described in Oteo et al. (2016).

A set of ALMA images are shown in Fig. 1. The core is detected at all bands. All jet's components are clearly visible in bands 3, 4, 5. A robust detection up to band 8 can be reported for the JBF, while knot1, knot2, and the jet termination progressively faint in bands 6 to 7 and only knot1 is marginally ($\sim 3\sigma$) detected also in band 8.

The integrated flux densities and peak brightness of the compact components were measured fitting 2D Gaussian functions with the `imfit` task in the Common Astronomy Software Applications (CASA), version 6.2.0.124. The errors on the flux measurements were calculated adding in quadrature the statistical errors from the fit and the calibration errors. Following the prescriptions in the ALMA guide (Cortes et al. 2020), we assumed a 5 per cent uncertainty in the flux calibration for bands 3, 4, and 5 and 10 per cent for bands 6, 7, and 8.[6] In a few cases, we noted a significant difference in the flux densities for couples of observations performed in the same band and central frequency. In these observations, we measured higher integrated flux densities and lower ones at the peak. Given that the same trend is observed in all the features, an intrinsic flux variation was ruled out. We did not identify any obvious issue with the data reduction and calibration. However, convolving the images with a common beam with the `imsmooth` task, the largest beam for each couple of images being compared, the peak brightness are consistent within the uncertainties and the discrepancy between the integrated flux densities is reduced. For completeness, we still report the flux measurements from these observations in Table 4 but we retain them as less reliable for the rest of the analysis. In addition, depending on the angular resolution of the observation, the emission of the first two knots can be at times blended with that of the nearby brightest features (core and JBF for knot1 and knot2, respectively, see for example Fig. 5), inducing some level of noisiness in the flux measurements. Finally, not all the jet features were detected in each observation, depending on the angular resolution and rms. Upper limits in the higher bands, band 7 and 8, are relevant for the goals of our study in order to assess the presence of a turnover in the continuum emission (see Section 7) and were set at 3σ noise level.

6.2 Legacy survey

In the optical band, the field of J1512+02 has been observed as part of the SDSS[7] (York et al. 2000) and within the DESI Legacy Imaging Surveys[8] (Dey et al. 2019). The latter consist of three surveys aimed at obtaining improved photometry and morphologies of the SDSS spectroscopic galaxies in three (g, r, z) of the five (u, g, r, i, z) SDSS bandpasses. Specifically, the field of J1512+02 was imaged as part of the Dark Energy Camera Legacy Survey (DECaLS), using the Dark Energy Camera at the 4 m Blanco Telescope at the Cerro Tololo Inter-American Observatory (see Dey et al. 2019, for details).

Sky-subtracted, calibrated images of the field of J1512+02 were retrieved from the archives of these surveys. These are *u, g, r, i*, and *z* SDSS images (Ahn et al. 2012) and *g, r*, and *z* DECaLS images. The three DECaLS images were obtained by stacking of images taken between 2014 and 2018 August. A point-like source is visible at the location of the core in all SDSS images, which in bands *g*, *r*, *i*, and *z* appears surrounded by faint, diffuse emission, most likely associated to the host galaxy. No emission is significantly detected at the location of the jet. In each band, the flux upper limits of the jet features were measured in aperture photometry, using the same regions defined in the X-ray images (see Fig. 2). The flux upper limits are reported in Table 5.

The three DECaLS images are shown in Fig. 6. The emission of the host galaxy is clearly present: putative emission from the first two jet knots, which is not evident in the images, would be blended with the galaxy contribution. Beyond knot2 ($\gtrsim$6 arcsec from the core), the galaxy emission drastically decreases, in particular in the *g*-band image, and a knotty-like component emerges at the location of the JBF in the images of all three filters. The flux densities in the three bands were measured from the X-ray extraction region, choosing a background region located at the same distance from the central, dominant source (see Table 5). The excess in brightness of this feature is slightly above twice the signal measured in a semicircular sector at the same distance from the centre of the jet feature. Because of this, given the presence of other, although fainter, blobs around the galaxy, we consider this as a tentative, rather than a conclusive, optical detection. Sensitive, optical-UV observations, for example, using the *Hubble Space Telescope* (*HST*), could confirm the detection. No flux excess is evident in the jet termination region and we report the upper limits in Table 5.

7 SEDS OF THE JET STRUCTURES

In the J1512+02 jet, we observed bright, compact features and faint, diffuse emission from the radio to the X-ray band. The SEDs of the main four jet components, shown in Fig. 7, display some remarkable characteristics. (i) The SEDs of knot1, knot2, and JBF clearly show that the radiative output is greater in X-rays than in the radio-to-sub-mm band. In particular, for knot1 and JBF the X-ray (1 keV) to radio (5 GHz) luminosity ratios, L_X/L_r, are $\sim$51 and $\sim$16, respectively. (ii) The ALMA fluxes of the JBF and jet termination mark a turnover, with a rapid drop of the emission in the $\sim$200–460 GHz range. This holds true even if we consider only the ALMA peak fluxes. The ALMA fluxes coupled with the non-detections in the optical band require at least two radiative components to describe the radio-to-X-ray SEDs of these two jet features. Intriguingly, a confirmation of the optical detection would add further complexity to the SED of JBT, as the DECaLS data points may imply even a third radiative component. (iii) The SEDs of knot1 and knot2 are still compatible with a single, radio-to-X-ray spectral component. However, the ALMA fluxes of knot2, and to less extent those of knot1, appear in excess over the interpolation between the radio and X-ray data points (see Fig. 7). This could be partially ascribed to some level of contamination from the diffuse emission surrounding the two knots. However, we note that the excess is still present, in particular in knot2 SED, when we use the ALMA peak fluxes.

[5] https://almacal.wordpress.com/
[6] https://almascience.nrao.edu/documents-and-tools/cycle8/alma-proposers-guide
[7] https://www.sdss.org/
[8] https://www.legacysurvey.org/

Table 3. ALMA observation log.

ObsID	Date YYYY/MM/DD/hh:mm:ss	Band	ν GHz	rest. beam arcsec^2	PA deg.
(1)	(2)	(3)	(4)	(5)	(6)
Xc02418_X78c9	2017/05/10/02:39:31	B3	97.49	0.91 × 0.71	54.0
Xbc9c9e_X21bb	2017/01/07/12:35:09	B3	107.56	2.92 × 2.10	− 67.5
Xbc9c9e_X26fa	2017/01/07/13:55:53	B3	107.56	3.37 × 2.05	− 61.8
Xbcef34_X292e	2017/01/21/10:23:50	B4	156.74	2.09 × 1.51	70.2
Xbd9424_Xd65	2017/03/05/07:42:03	B4	156.74	2.48 × 1.75	59.5
Xd12f5c_X7bc8	2018/08/28/00:11:20	B5	199.90	1.55 × 0.63	− 66.3
Xda845c_X15e5b	2019/04/10/07:46:52	B5	200.59	1.36 × 0.84	− 81.2
Xdab261_X10376	2019/04/13/07:16:04	B5	200.59	1.08 × 0.80	− 80.3
Xbb968f_X37c7	2016/12/10/12:00:34	B6	238.24	0.77 × 0.64	52.7
Xe1f219_X6963$^{(*)}$	2019/10/08/18:02:50	B6	236.32	0.55 × 0.52	14.8
Xe20b32_X4892$^{(*)}$	2019/10/10/17:17:20	B6	236.32	0.56 × 0.50	70.1
Xcd8029_Xbd79	2018/05/18/04:54:20	B7	343.50	1.09 × 0.97	− 82.6
Xce3de5_Xbec	2018/06/03/02:37:17	B7	290.17	1.42 × 0.82	− 73.1
Xce1e34_X63b7	2018/06/01/04:20:05	B7	299.73	1.12 × 1.00	− 73.8
Xe20b32_X4c48$^{(*)}$	2019/10/10/18:32:19	B7	343.50	0.40 × 0.35	− 63.5
Xe20b32_X532c$^{(*)}$	2019/10/10/20:21:32	B7	298.37	0.58 × 0.38	− 61.3
Xcdd033_X2726	2018/05/24/04:38:31	B8	465.52	0.82 × 0.61	− 62.3
Xce1e34_X696d	2018/06/01/03:26:56	B8	401.40	0.87 × 0.71	− 65.4

Notes. Columns: (1) ALMA observation ID; (2) observing time; (3) & (4) ALMA band and frequency; (5) & (6) restoring beamsize and position angle. $^{(*)}$: these observations should be considered with caution as the integrated flux densities of all jet components appear systematically higher and the peak brightness lower.

7.1 Jet SED modelling

We assumed a pure leptonic scenario, and modelled the SEDs with a simple, synchrotron, and IC one-zone model. The emission of each component is produced in a region of spherical shape and radius $R^{'}$ (where primed quantities indicate the jet's comoving frame). The spherical volume is uniformly filled by relativistic plasma (i.e. a filling factor equal one was assumed) and magnetic field, $B^{'}$. The energy densities of relativistic leptons and magnetic field are $U^{\prime}_{e}$ and $U^{\prime}_{B}$, respectively. The region is moving with a bulk Lorentz factor $\Gamma_{\rm bulk}$ and θ is the angle between the jet axis and the observer's line of sight.

The electrons radiate via the synchrotron mechanism. The locally produced synchrotron photons and the CMB photons provide the seed photons for the IC mechanism. At the knot1 scales and beyond, $\gtrsim$8 kpc (projected), the densities of nuclear photons from the AGN (i.e. direct and reprocessed disc emission) are negligible. If we correct their distances for projection effects (a factor $\geq$2 for $\theta \leq 30^{\circ}$), the jet's features appear to be located out of the host galaxy bulge. Therefore, we do not expect that upscattering of the stellar photons can represent an important contribution to the IC emission. We then focused on two scenarios: in the first, the dominant contribution to the X-ray emission of each jet component is SSC (model X-ray$_{\rm SSC}$ in Table 6), while, in the second, it is the IC/CMB process (model X-ray$_{\rm IC/CMB}$ in Table 6). In addition, for knot1 and knot2 we also discuss the case of a single radio-to-X-ray synchrotron component (X-ray$_{\rm synch}$ model), which is still consistent with the observed SEDs.

Rough constraints on the maximum sizes of the emitting regions were derived from the radio measurements (see Section 4). For knot1 and knot2, we used a reference maximum value, $R = 100$ pc. The electrons' energy distribution (EED) between the minimum and maximum Lorentz factors ($\gamma^{\prime}_{min}$ and $\gamma^{\prime}_{max}$, respectively) was assumed to have the simplest shape of a single power-law for all cases except when we applied the X-ray$_{\rm synch}$ model to the knot2 SED, which requires a broken power law to be described by a single radiative component. The EED spectral index for the single power-law case was derived from the radio spectral index ($p = 2\alpha_r + 1$), with tolerance to vary within the uncertainties. Note that this choice worked well also for the X-ray$_{\rm synch}$ model of knot1. We allowed $\gamma^{\prime}_{min}$ to range between minimum, standard values ($\sim$10), and the maximum value allowed by the SED. In the SEDs of JBF and jet termination, the turnover in the ALMA band sets the limits to $\gamma^{\prime}_{max}$. In knot1 and knot2, $\gamma^{\prime}_{max}$ was simply adjusted to the minimum value needed to reproduce the observed SED according to the specific scenario. The high-energy emission of the jet components should also not overpredict the observed γ-ray flux (see the *Fermi* data points reported in the JBF SED in Fig. 7).

Clearly, for the assumed spectral shape of the EED, the value of $\gamma^{\prime}_{min}$ can significantly modify the estimates of the jet kinetic power, while $\gamma^{\prime}_{max}$ is relevant for the jet's radiated power.

For each set of jet parameters we inferred the jet's bolometric radiative power, L_r, and the jet power, $L_{\rm jet}$, given by the sum of the Poynting flux, L_B and the kinetic power, $L_{\rm kin}$ (see e.g. Zdziarski 2014). The latter is the sum of the powers of the relativistic leptons, L_e and of the protons, L_p. We assumed one cold proton per relativistic electron. The jet parameters and jet powers for the models are reported in Table 6. We stress that, given the limited data set, there is not an unique set of parameters that can reproduce the observed SEDs. However, the values reported in the table can be considered as representative of a family of similar solutions and can be used to illustrate the jet properties for one or the other process being responsible for the X-ray emission.

Some main results of the modelling are common to all jets' features and basically independent from the assumptions. First, under the condition of energy equipartition between particles and magnetic field, $U^{\prime}_{e} \sim U^{\prime}_{B}$ (calculated for the given $\gamma_{\rm min}$), SSC underestimates by several orders of magnitude the observed X-ray emission. Compact regions and $U^{\prime}_{e}/U^{\prime}_{B} \gg 1$ are needed to reach the observed fluxes. For example, in knot1 an emitting region of $\sim$3.5 pc, for $\Gamma_{\rm bulk} = 4$ and

Table 4. ALMA fluxes.

ν (GHz) (1)	F_ν (mJy) (2)	F_{peak} (mJy beam^{-1}) (3)	beam-decov. size (arcsec^2) (4)	Band (5)	ObsID (6)
			Core		
97.49	282 ± 14.1	282 ± 14	0.02 × 0.01	B3	Xc02418_X78c9
107.56	178 ± 9	178 ± 9	unresolved	B3	Xbc9c9e_X21bb
107.56	190 ± 9	190 ± 9	unresolved	B3	Xbc9c9e_X26fa
156.74	193 ± 10	193 ± 10	0.09 × 0.04	B4	Xbcef34_X292e
156.74	271 ± 13	271 ± 13	unresolved	B4	Xbd9424_Xd65
199.90	271 ± 13	271 ± 13	unresolved	B5	Xd12f5c_X7bc8
200.59	228 ± 11	228 ± 11	<0.04 × 0.01	B5	Xda845c_X15e5b
200.59	217 ± 11	217 ± 11	<0.05 × 0.02	B5	Xdab261_X10376
236.32	273 ± 27	273 ± 27	unresolved	B6	Xe20b32_X4892(*)
236.32	264 ± 26	264 ± 26	unresolved	B6	Xe1f219_X6963(*)
238.24	125 ± 12	125 ± 12	unresolved	B6	Xbb968f_X37c7
290.17	231 ± 23	227 ± 23	0.18 × 0.10	B7	Xce3de5_Xbec
298.37	245 ± 24	245 ± 25	unresolved	B7	Xe20b32_X532(*)
299.73	215 ± 21	215 ± 22	unresolved	B7	Xce1e34_X63b7
343.50	224 ± 22	224 ± 22	0.07 × 0.02	B7	Xcd8029_Xbd79
343.50	254 ± 25	254 ± 25	unresolved	B7	Xe20b32_X4c48(*)
401.40	206 ± 21	207 ± 21	unresolved	B8	Xce1e34_X696d
465.52	226 ± 23	225 ± 22	0.04 × 0.03	B8	Xcdd033_X2726
			knot1		
97.49	3.1 ± 0.7	1.0 ± 0.2	1.24 × 0.50	B3	Xc02418_X78c9
199.90	0.6 ± 0.1	0.74 ± 0.09	unresolved	B5	Xd12f5c_X7bc8
200.59	0.8 ± 0.3	0.6 ± 0.1	unresolved	B5	Xda845c_X15e5b
200.59	1.2 ± 0.3	0.7 ± 0.1	1.03 × 0.41	B5	Xdab261_X10376
236.32	2.7 ± 0.5	0.40 ± 0.05	1.90 × 0.80	B6	Xe20b32_X4892(*)
236.32	4.8 ± 0.9	0.43 ± 0.07	2.05 × 1.42	B6	Xe1f219_X6963(*)
238.24	1.0 ± 0.2	0.7 ± 0.1	0.48 × 0.31	B6	Xbb968f_X37c7
299.73	0.7 ± 0.2	0.5 ± 0.1	unresolved	B7	Xce1e34_X63b7
343.50	0.9 ± 0.3	0.5 ± 0.1	<1.1 × 0.1	B7	Xe20b32_X4c48(*)
465.52	0.5 ± 0.2	0.54 ± 0.1	<0.8 × 0.6	B8	Xcdd033_X2726
			knot2		
200.59	0.8 ± 0.3	0.6 ± 0.1	unresolved	B5	Xda845c_X15e5b
236.32	1.6 ± 0.4	0.20 ± 0.05	2.00 × 0.96	B6	Xe20b32_X4892(*)
236.32	1.7 ± 0.4	0.6 ± 0.1	1.78 × 0.67	B6	Xe1f219_X6963(*)
299.73	0.6 ± 0.2	0.4 ± 0.1	unresolved	B7	Xce1e34_X63b7
343.50	0.8 ± 0.4	0.28 ± 0.09	unresolved	B7	Xe20b32_X4c48(*)
401.40	–	<0.9	–	B8	Xce1e34_X696d
465.52	–	<0.8	–	B8	Xcdd033_X2726
			Jet brightest feature		
97.49	18.2 ± 1.6	4.4 ± 0.4	1.92 × 1.01	B3	Xc02418_X78c9
107.56	11.9 ± 0.8	8.7 ± 0.5	1.97 × 0.27	B3	Xbc9c9e_X21bb
107.56	13.0 ± 0.8	9.1 ± 0.5	2.04 × 0.67	B3	Xbc9c9e_X26fa
156.75	8.2 ± 0.5	5.8 ± 0.3	1.46 × 0.55	B4	Xbcef34_X292e
156.74	7.8 ± 0.6	6.4 ± 0.4	unresolved	B4	Xbd9424_Xd65
199.90	8.3 ± 0.6	2.7 ± 0.2	1.48 × 1.12	B5	Xd12f5c_X7bc8
200.59	6.4 ± 0.5	3.1 ± 0.2	1.31 × 0.79	B5	Xda845c_X15e5b
200.59	7.0 ± 0.5	2.7 ± 0.2	1.34 × 0.95	B5	Xdab261_X10376
236.32	8.7 ± 1.0	1.5 ± 0.2	1.38 × 0.9	B6	Xe20b32_X4892(*)
236.32	8.9 ± 1.0	1.5 ± 0.2	1.35 × 1.02	B6	Xe1f219_X6963(*)
238.24	5.9 ± 0.7	2.0 ± 0.2	1.24 × 0.74	B6	Xbb968f_X37c7
290.17	3.6 ± 0.5	1.9 ± 0.2	1.23 × 0.40	B7	Xce3de5_Xbec
298.37	6.0 ± 0.7	0.9 ± 0.1	1.17 × 1.00	B7	Xe20b32_X532c(*)
299.73	3.3 ± 0.4	2.0 ± 0.2	1.03 × 0.62	B7	Xce1e34_X63b7
343.50	3.0 ± 0.5	1.5 ± 0.2	1.23 × 0.75	B7	Xcd8029_Xbd79
343.50	4.2 ± 1.1	0.8 ± 0.1	0.93 × 0.75	B7	Xe20b32_X4c48(*)
401.40	2.9 ± 0.8	1.1 ± 0.2	1.33 × 0.67	B8	Xce1e34_X696d
465.52	2.0 ± 0.6	0.6 ± 0.1	1.58 × 0.65	B8	Xcdd033_X2726
			Jet termination		
97.49	12.1 ± 1.3	1.6 ± 0.2	3.15 × 1.33	B3	Xc02418_X78c9
107.56	7.5 ± 0.7	4.8 ± 0.3	2.38 × 0.94	B3	Xbc9c9e_X21bb

Table 4 – *continued*

ν (GHz) (1)	F_ν (mJy) (2)	F_{peak} (mJy beam^{-1}) (3)	beam-decov. size (arcsec^2) (4)	Band (5)	ObsID (6)
107.56	8.5 ± 0.8	4.9 ± 0.4	2.64 × 1.38	B3	Xbc9c9e_X26fa
156.74	4.2 ± 0.4	2.3 ± 0.2	2.44 × 0.79	B4	Xbcef34_X292e
156.74	4.4 ± 0.5	2.9 ± 0.3	2.21 × 0.96	B4	Xbd9424_Xd65
199.90	3.4 ± 0.5	0.8 ± 0.1	1.99 × 1.30	B5	Xd12f5c_X7bc8
200.59	3.0 ± 0.6	0.8 ± 0.1	2.6 × 0.4	B5	Xda845c_X15e5b
200.59	3.4 ± 0.5	0.9 ± 0.1	2.1 × 1.2	B5	Xdab261_X10376
236.32	7.4 ± 1.3	0.24 ± 0.04	4.3 × 1.9	B6	Xe20b32_X4892$^{(*)}$
236.32	5.9 ± 1.3	0.22 ± 0.05	4.8 × 1.5	B6	Xe1f219_X6963$^{(*)}$
238.24	2.0 ± 0.7	0.34 ± 0.09	1.9 × 1.3	B6	Xbb968f_X37c7
290.17	1.0 ± 0.5	0.4 ± 0.1	2.2 × 0.2	B7	Xce3de5_Xbec
299.73	0.6 ± 0.2	0.4 ± 0.1	unresolved	B7	Xce1e34_X63b7
401.40	–	<0.9	–	B8	Xce1e34_X696d
465.52	–	<0.8	–	B8	Xcdd033_X2726

Notes. Columns: (1) observing frequency; (2) integrated flux density; (3) peak brightness; (4) beam-deconvolved size assuming a Gaussian model; (5) observing band; (6) ALMA observation ID. Uncertainties in (2) and (3) include the fit error and the calibration error. $^{(*)}$: flux densities measurements in these observations appear systematically higher and the peak brightness lower (see the text).

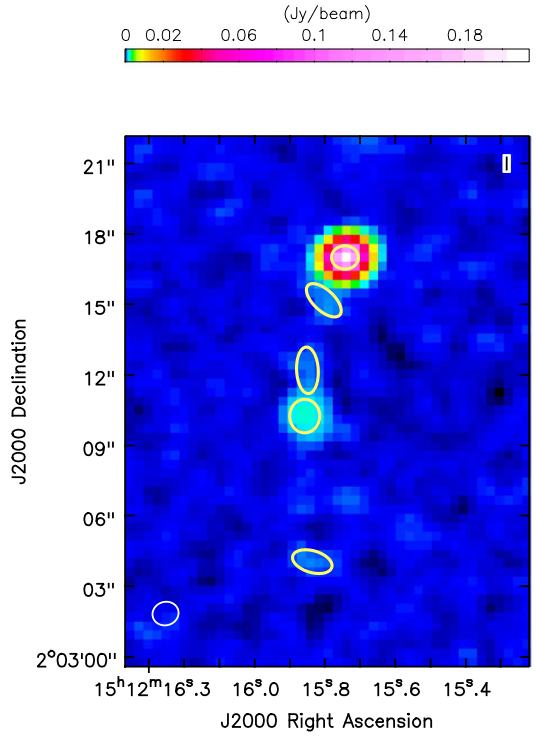

Figure 5. ALMA band 7 (299.7 GHz) image of observation Xce1e34_X63b7 and fit of the core and jet components (see Tables 3 and 4).

$\theta = 5^\circ$ still requires $U'_e/U'_B \gtrsim 10^9$ and B' ∼4–5 μG. Note that the IC/CMB luminosity for this model peaks at $\gtrsim 10^{21}$ Hz (≈10^{43} erg s^{-1}) and remains largely subdominant in X-rays (see Fig. 7). The need for a particle dominated region does not depend on $\Gamma_{\rm bulk}$ and θ. In fact, it holds true also for the JBF ($U'_e/U'_B \gtrsim 10^5$), under the assumption of a mildly or subrelativistic motion: we tested the case for $\beta = 0.2$, where β is the jet speed in units of speed of light c ($\Gamma_{\rm bulk} = 1.02$), a value within the range of velocities estimated for the hotspots (see O'Dea et al. 2009; Kappes et al. 2019). This is not surprising, given the same dependence of both, synchrotron and SSC luminosities, on the Doppler factor,[9] δ, $L \propto \delta^4 L'$, where $\delta = (\Gamma_{\rm bulk}(1 - \beta\cos\theta))^{-1}$. Similarly, the increase of $\gamma_{\rm min}$ has only a moderate impact on the U'_e/U'_B ratio. The same considerations on SSC are valid also for the other two jet features, knot2 and jet termination.

Secondly, for $U'_B \sim 0.1$–$0.8U'_e$, the observed X-ray luminosities can be ascribed to IC/CMB emission on condition of a highly relativistic ($\Gamma_{bulk} \gtrsim 5$) jet seen at $\theta \lesssim 5^\circ$. The magnetic field in the jet regions is ≈20 μG, similar to values found in several jets (e.g. Kataoka & Stawarz 2005). For these parameters, the estimated jet powers of the IC/CMB model in the jet features are similar $L_{\rm jet} \sim 10^{44}$–10^{45} erg s^{-1} depending on the assumed $\gamma_{\rm min}$. For smaller values of $\Gamma_{\rm bulk}$, U'_e must be larger, hence changing the energy balance between particles and magnetic field. For example, in the jet termination $\Gamma_{\rm bulk} \leq 1.4$ requires $U'_e/U'_B \geq 10^3$ and jet powers larger than 10^{46} erg s^{-1}.

Last, the effects of varying $\gamma_{\rm min}$ are evident comparing the two SSC models considered for knot1: when $\gamma_{\rm min}$ is set to the maximum value allowed by the data (X-ray$_{\rm SSC,\,2}$ in Table 6), L_p significantly decreases and the kinetic power is reduced by more than an order of magnitude with respect to its value for $\gamma_{\rm min} \sim 10$ (X-ray$_{\rm SSC,\,1}$). Leaving unchanged the other model parameters, within the IC scenario (SSC or IC/CMB) $\gamma_{\rm max}$ must be $\lesssim 10^6$ for the knot1 and knot2 not to exceed the observed optical upper limits and γ-ray flux. For these maximum values, L_r still represents a limited fraction ($\leq$0.1) of the total jet power. In the case of the JBF and jet termination, the observed turnover in the ALMA bands set $\gamma_{\rm max} < 10^5$.

Finally, we discuss the X-ray$_{\rm synch.}$ models of knot1 and knot2. The radio to X-ray SED can be ascribed to a single synchrotron component under condition of energy equipartition and jet powers within a few 10^{44} erg s^{-1}, i.e. lower than the IC models, however, a high $\gamma_{\rm max}$, $\sim 10^8$, is needed. The X-ray$_{\rm synch.}$ model of knot2 requires a broken power law, though the present data set leaves the break energy and the value of the slope beyond the break largely unconstrained.

[9]Note that in the case of IC off an external radiation field (such as IC/CMB) the dependence is $\propto \delta^6/\Gamma^2_{bulk}$ (Dermer 1995).

Table 5. Aperture photometry infrared and optical flux densities and upper limits measured in SDSS and DECaLS images.

Component	g	u	r	i	z
	erg cm^{-2} s^{-1} Hz^{-1}	erg cm^{-2} s^{-1} Hz^{-1}	erg cm^{-2} s^{-1} Hz^{-1}	erg cm^{-2} s^{-1} Hz^{-1}	erg cm^{-2} s^{-1} Hz^{-1}
(1)	(2)	(3)	(4)	(5)	(6)
			SDSS		
knot1	$<4.9 \times 10^{-29}$	$<9.8 \times 10^{-30}$	$<1.0 \times 10^{-28}$	$<2.2 \times 10^{-28}$	$<2.0 \times 10^{-28}$
knot2	$<1.0 \times 10^{-29}$	$<9.1 \times 10^{-30}$	$<2.4 \times 10^{-29}$	$<3.0 \times 10^{-29}$	$<4.0 \times 10^{-29}$
Jet brightest feature	$<2.9 \times 10^{-29}$	$<1.2 \times 10^{-29}$	$<3.6 \times 10^{-29}$	$<4.0 \times 10^{-29}$	$<1.7 \times 10^{-28}$
jet termination	$<8.7 \times 10^{-30}$	$<6.5 \times 10^{-30}$	$<2.6 \times 10^{-29}$	$<3.1 \times 10^{-29}$	$<2.0 \times 10^{-28}$
			Legacy Surveys – DECaLS		
Jet brightest feature$^{(*)}$	1.3×10^{-29}	–	2.2×10^{-29}	–	3.9×10^{-29}
jet termination	$<1.3 \times 10^{-29}$	–	$<2.5 \times 10^{-29}$	–	$<2.9 \times 10^{-29}$

Notes. Columns: (1) jet components, the filters from (2) to (6) correspond to the following median frequencies: 6.3×10^{14} Hz, 8.47×10^{14} Hz, 4.82×10^{14} Hz, 3.93×10^{14} Hz, and 3.31×10^{14} Hz. $^{(*)}$: 2σ level detection.

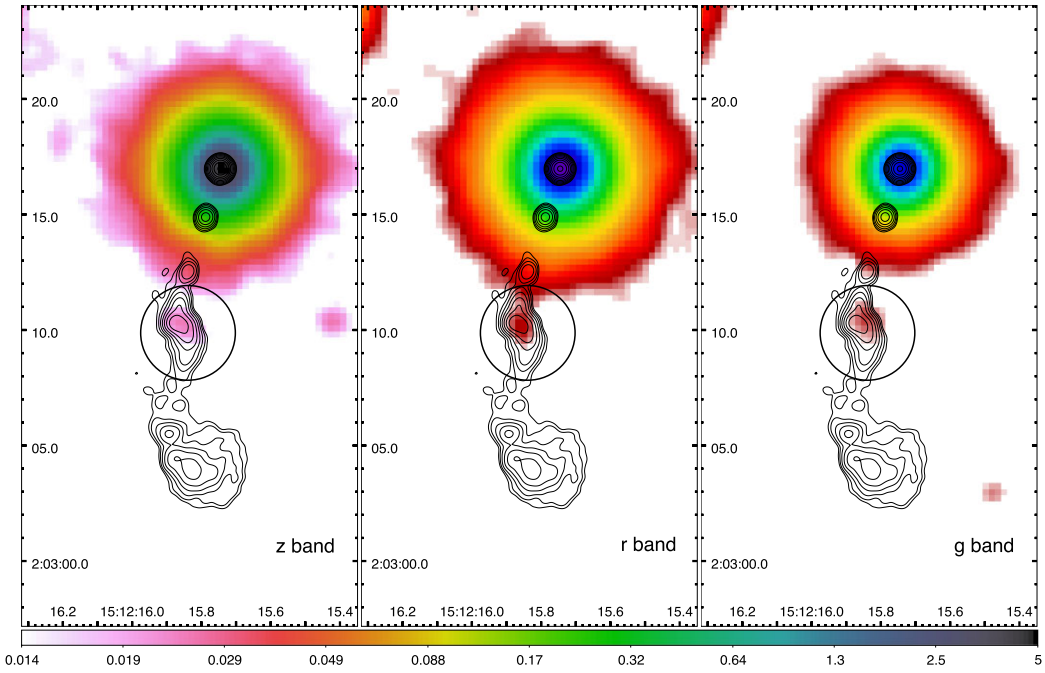

Figure 6. DECam images of J1512+02 taken with the *z* (left-hand panel), *r* (centre), and *g* (right-hand panel) filters with overlaid 4.9 GHz radio contours. The pixel scale is ∼0.262 arcsec pixel^{-1}. The colour scale is logarithmic and in units of nanomaggy. For each band, the minimum of the scale is set to 2 × rms. The region corresponding to the jet brightest feature is marked by the black circle. The images have been retrieved from the website of the DESI Legacy Imaging Surveys.

The model is equally feasible for lower bulk motions ($\Gamma_{\rm bulk}$ ∼2) and larger viewing angles (θ ∼20°), by varying the volume of the emitting regions within the upper limits from observations (see X-ray$_{\rm synch.,\,2}$ of knot1 in Table 6) and with an increase of the jet energy budget within a factor of ∼2.

8 DISCUSSION

In J1512+02 the different morphology, intensity, and SEDs of the jet features suggest diverse radiative and/or particle acceleration mechanisms at work. First, we critically discuss the models, and the required jet parameters' values, in light of the implications for the jet's stability, dynamics, and energetics. Then, the observable properties and SED of the J1512+02 jet are compared to other well-studied X-ray jets.

8.1 SSC, IC/CMB, and synchrotron: implications for the jet physics

In the SSC scenario, the large, even extreme, U_e/U_B ratios point to a jet that is particle-dominated on kiloparsec scales. Very-long-baseline interferometry (VLBI), probing the innermost parts of the jets, has provided evidence that the acceleration and collimation phase is completed within tens of parsec distances from the black hole (see Boccardi et al. 2021, and references therein). At these scales, the combined action of the jet's magnetic field and of the ambient medium would concur to the jet's collimation. According to theoretical models and simulations, during this first phase, some mechanism, yet poorly known, would mediate the conversion of (a fraction of) the jet's magnetic energy into kinetic power. The outlined scenario provides some support to a jet that is particle-dominated at kiloparsec scales. None the less, for the large U_e/U_B ratios of the SSC scenario, the jet would be highly overpressured, at least locally

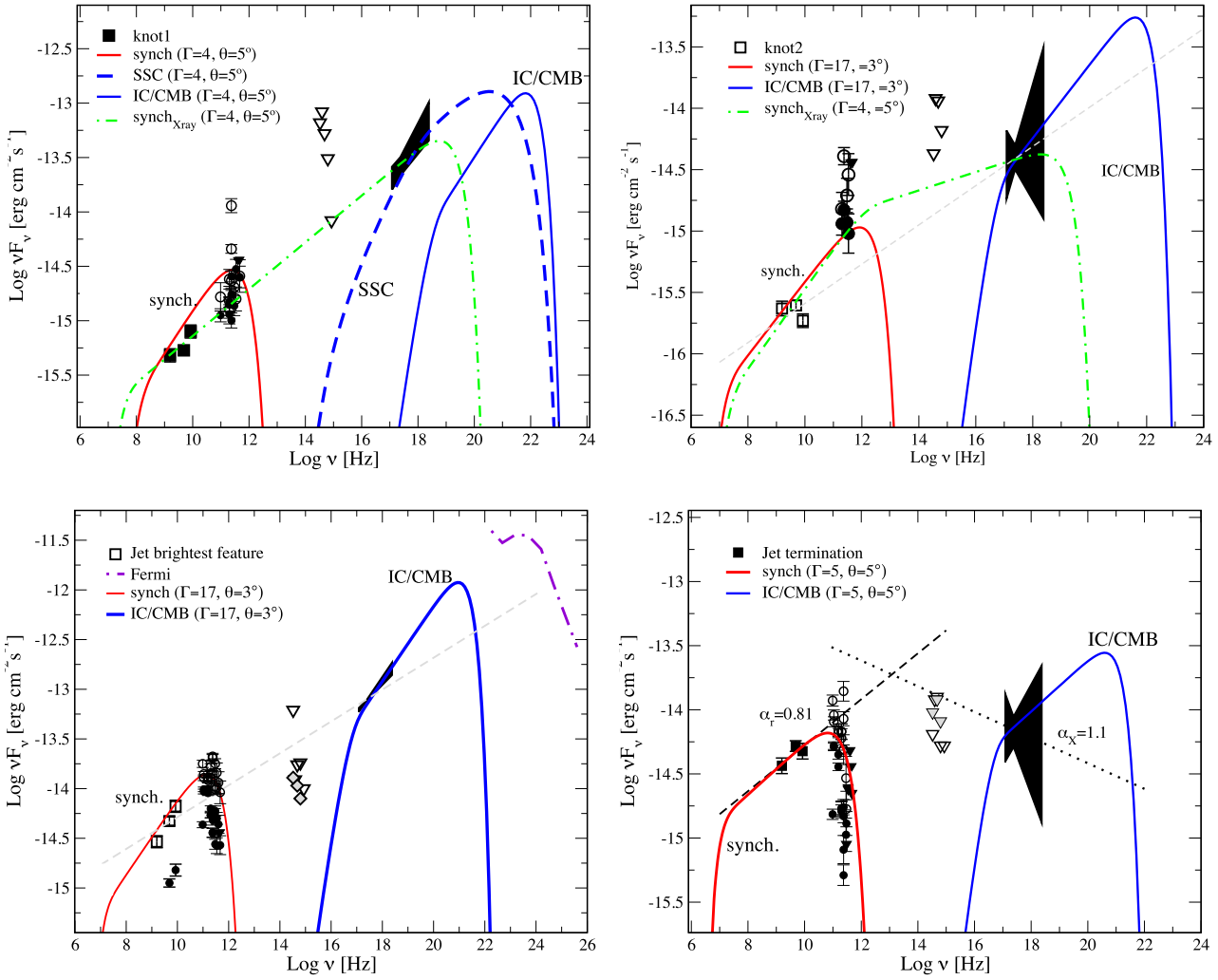

Figure 7. Observed SEDs and models of the main features of the J1512+02 jet. We plot the ALMA integrated fluxes (empty circles) and the peak fluxes (filled circles). Similarly, for the JBF, both the radio fluxes of the extended region (empty squares) and the peak fluxes (filled squares) are shown. Triangles are upper limits: empty triangles are the SDSS upper limits while the grey ones are measured from the DECaLS data. In the JBF SED, the grey diamonds correspond to the tentative DECaLS detection, while the dot-dashed line indicates the γ-ray emission detected by *Fermi* (see the text). For knot1 (upper left-hand panel), we show the SSC model (X-ray$_{SSC,\,2}$ in Table 6) and the single synchrotron model (X-ray$_{synch.,\,1}$ in Table 6). For knot2 (upper right-hand panel), we show the IC/CMB model (X-ray$_{IC/CMB}$ in Table 6) and the single synchrotron model (X-ray$_{synch.}$ in Table 6). For the JBF, we show the IC/CMB model (X-ray$_{IC/CMB}$ in Table 6) and for the jet termination the IC/CMB model (X-ray$_{IC/CMB,\,1}$ in Table 6). The grey dashed lines in the knot2 and JBF SEDs are the interpolation between the radio and X-ray fluxes. In the jet termination SED, the dashed (dotted) line is the best-fitting slope of the radio (X-ray) data.

at the scales of the emitting regions. If not the magnetic field, another agent should intervene and prevent the jet's disruption. In fact, the pressure exerted by the ambient gas, either in the hot haloes of the host galaxies or in galaxies' clusters, is typically in the range $\sim 10^{-12}$–10^{-11} erg cm^{-3}, thus largely below the inferred internal pressure (for knot1 $p_{\rm knot1} \sim U'_e/3 \sim 10^{-4}$ erg cm^{-3}). Yet, J1512+02's jet appears collimated at least up to the JBF.

The large jet powers are a second critical issue for the SSC model. This is true in particular for the knot1: its total jet power exceeds 10^{47} erg s^{-1} (see Table 6), even for a $\gamma_{\rm min}$ that minimizes $L_{\rm kin}$. By excluding the presence of an hadronic component, whose actual contribution in jets, if any, is not clearly established (e.g. Celotti & Ghisellini 2008), the bulk of the power would be carried by relativistic leptons ($L_e \sim 9 \times 10^{46}$ erg s^{-1}). However, we must note that the maximum values of $\gamma_{\rm min}$ assumed here ($\sim$500–1000) to minimize the jet power are rather high, while particle in cell simulations of relativistic shocks in magnetized electron-ion plasma find $\gamma_{\rm min}$ typically $\lesssim 100$ (e.g. Spitkovsky 2008; Sironi & Spitkovsky 2011).

For a comparison, we derived the jet power in two alternative ways. The first method is based on the empirical relation proposed by Willott et al. (1999) between the jet power and the radio luminosity:

$$L_{\rm jet,151}[\rm erg\ s^{-1}] = 5 \times 10^{22} f^{3/2} (L_{1.4}[\rm W\ Hz^{-1}])^{6/7}, \quad (1)$$

where $L_{1.4}$ is the monochromatic radio power at 1.4 GHz.[10] In the revised expression considered here, a factor f takes into account possible, systematic underestimates intrinsic to the technique, estimated to be in the range between 10 and 20 for a sample of FRI and FRII sources (Hardcastle, Evans & Croston 2007b; Fernandes et al. 2011).

[10]Here, we used the 1.4 GHz luminosity assuming a radio spectral index of 0.8 between 151 MHz and 1.4 GHz (e.g. Rusinek et al. 2017).

Table 6. SED models and input parameters.

Model	$R^{'}$	$B^{'}$	$\gamma'_{\rm min}/\gamma'_{\rm max}$	p	$\Gamma_{\rm bulk}$	θ	(U'_B/U'_e)	L_r	L_B	L_e	L_p
	pc	μG				deg.		erg s^{-1}	erg s^{-1}	erg s^{-1}	erg s^{-1}
(1)	(2)	(3)	(4)	(5)	(6)	(7)	(8)	(9)	(10)	(11)	(12)
					knot1						
X-ray$_{\rm SSC,\,1}$	3.5	4	$10/8 \times 10^4$	2.2	4	5	5×10^{-10}	2×10^{42}	3×10^{38}	4×10^{47}	8×10^{48}
X-ray$_{\rm SSC,\,2}$	3.5	4.5	$1 \times 10^3/8 \times 10^4$	2.2	4	5	1×10^{-10}	2×10^{42}	3×10^{38}	9×10^{46}	3×10^{46}
X-ray$_{\rm IC/CMB}$	100	15	$50/2.5 \times 10^4$	2.35	18	2	0.1	1×10^{41}	7×10^{43}	2×10^{44}	1×10^{45}
X-ray$_{\rm synch.,\,1}$	100	100	$100/1 \times 10^8$	2.57	4	5	1	3×10^{41}	1×10^{44}	4×10^{43}	1×10^{44}
X-ray$_{\rm synch.,\,2}$	170	160	$100/1 \times 10^8$	2.57	2	20	0.8	4×10^{42}	2×10^{44}	9×10^{43}	2×10^{44}
					knot2						
X-ray$_{\rm IC/CMB}$	100	26	$80/4 \times 10^4$	2.4	17	3	0.6	7×10^{40}	2×10^{44}	8×10^{43}	4×10^{44}
X-ray$_{\rm synch.}$	100	70	$100/1 \times 10^8$	2.35/2.85	4	5	0.8	6×10^{40}	7×10^{43}	3×10^{43}	7×10^{43}
					Jet brightest feature (JBF)						
X-ray$_{\rm SSC}$	25	100	$500/3.5 \times 10^4$	2.1	1.02	25	7×10^{-6}	3×10^{43}	1×10^{41}	4×10^{45}	6×10^{43}
X-ray$_{\rm IC/CMB}$	250	18	$80/1.8 \times 10^4$	2.24	17	3	0.2	1×10^{42}	6×10^{44}	8×10^{44}	3×10^{45}
					Jet termination						
X-ray$_{\rm IC/CMB,\,1}$	1×10^3	22	$100/2.1 \times 10^4$	2.6	5	5	0.8	1×10^{41}	1×10^{45}	4×10^{44}	2×10^{45}
X-ray$_{\rm IC/CMB,\,2}$	3×10^3	4	$100/8 \times 10^4$	2.6	1.4	5	2.5×10^{-4}	1×10^{42}	2×10^{43}	2×10^{46}	3×10^{46}

Notes. (1) model; (2) radius of the emitting region; (3) magnetic field; (4) minimum, maximum Lorentz factors of the EED; (5) spectral index of the EED; (6) bulk Lorentz factor; (7) angle between the main jet axis and the observer viewing angle; (8) ratio between the energy densities of the magnetic field and relativistic particles; (9) bolometric radiative power; (10) Poynting flux; (11) & (12) kinetic power in electrons and protons, respectively, assuming one cold proton per relativistic electron.

The 1.4 GHz integrated flux density from the FIRST survey is 0.88 Jy. Note that this measurement is in agreement with the extrapolation to this frequency of the 74 MHz flux if a spectral index of 0.8 is assumed, thus allowing us to exclude that the FIRST flux is boosted by relativistic effects. With this flux density, we obtained $L_{\rm jet,\,151} \sim 4 \times 10^{44}$ erg s^{-1} for $f = 10$, and $L_{\rm jet,\,151} \sim 1.2 \times 10^{45}$ erg s^{-1} for $f = 20$.

A further estimate of the jet power comes from the SED modelling of the γ-ray emitting core (see Section 1.1). Modelling of the broad-band emission of the core with an SSC and external Compton model returns $L_{\rm jet}$ between $\approx 10^{44}$ erg s^{-1} and $\approx 10^{46}$ erg s^{-1}, where the range takes into account the uncertainties on some parameters such as $\gamma_{\rm min}$ or, again, the jet's composition (Migliori et al., in preparation). Similar results ($L_{\rm jet} \approx 10^{46}$ erg s^{-1}) have been previously reported for J1512+02 by Sbarrato et al. (2012).

Both approaches lead to a discrepancy with the $L_{\rm jet}$ inferred from the X-ray$_{\rm SSC}$ models of the knot1, unless we consider it to be the result of a past, episodic increase of the jet activity. For the black hole mass of $10^{8.84}$ M$_\odot$ reported in Sbarrato et al. (2012), the estimated Eddington luminosity of the source is $L_{\rm Edd} \sim 7 \times 10^{46}$ erg s^{-1}. Therefore, only the minimum $L_{\rm jet}$ of knot1 (without a significant contribution of the hadronic component) is consistent with the Eddington luminosity. Note however that the unsually faint UV continuum and weak emission lines (see Section 1.1) could indicate a sub-Eddington regime, thus $L_{\rm Edd}$ should be regarded as an upper limit. The $L_{\rm jet}$ obtained in the X-ray$_{\rm SSC}$ models for the JBF ($\approx 10^{44}$–10^{45} erg s^{-1}), assuming a subrelativistic speed, is instead in broad agreement with the values of the independent estimates. In conclusion, the SSC scenario seems disfavoured for the X-ray emission of the knot1 (and knot2), while it could still hold for the (and the jet termination) from the energetic point of view. In all components however, there is no easy way to overcome the problems of the large departure from energy equipartition conditions and of the confinement of the plasma.

The energy budget of the jet in the IC/CMB model ($L_{\rm jet} \lesssim 10^{46}$ erg s^{-1}) is less extreme than in the SSC-dominated scenario, in particular for the knot1. Once again, the estimated value could be even lower by assuming a different cold protons-to-electrons ratio (e.g. assuming one cold proton every ten relativistic leptons). Furthermore, being the seed photons from an external photon field, the IC/CMB can reproduce the SED with only a moderate dominance of U'_e over U'_B. On the other hand, it requires small viewing angles ($\theta \lesssim 5^\circ$) and a large bulk motion ($\Gamma_{\rm bulk} \gtrsim 15$ for all components except the jet termination, for which $\Gamma_{\rm bulk} \sim 5$ is sufficient), thus posing precise constraints on the jet linear size and dynamics.

For the viewing angle $\theta \sim 3^\circ$, the deprojected distance of the JBF from the core is ~570 kpc. Despite the considerable increase with respect to the apparent size, these dimensions are still within the typical range for classical radio galaxies ($\lesssim$0.7 Mpc). In addition, wide/all sky surveys have recently discovered hundreds of giant radio galaxies (GRGs) with sizes up to 3.5 Mpc (Dabhade et al. 2020), a large fraction of which appears still in an active phase. A revision of the number of GRGs would alleviate one of the arguments against the IC/CMB mechanism, based on the deficit of misaligned counterparts to the aligned, IC/CMB X-ray jets (Harris & Krawczynski 2006, and references therein).

The jet must be highly relativistic on hundreds of kiloparsec scales. Numerical simulations have shown that high power ($L_{\rm jet} \sim 10^{45}$ erg s^{-1}), highly relativistic ($\Gamma_{\rm bulk} = 10$) jets with a high density ratio with respect to their ambient medium can propagate within the galaxy cores (~600 pc) without undergoing significant deceleration (Rossi et al. 2020), which, however, could arise at even larger scales because of internal instabilities (Perucho, Martí & Quilis 2019; Mukherjee et al. 2020). Indeed, the morphology of J1512+02 supports a relativistic boosting of the emission. The radio structure is symmetric only in the FIRST image, at low frequency and low angular resolution, while we did not detect the counter-jet at any radio frequency or in the X-rays. The associated γ-ray emission is an additional indication of a jet that, at least on small scales, is relativistic and aligned with our line of sight. On the other hand, other parameters indicative of the source alignment, such as the core-to-total radio flux (see Section 1.1), do not fully support this picture. Giovannini et al. (1988) derived a general correlation between the core radio power at 5 GHz and the total radio power at 408 MHz in radio galaxies. From such relation, using the total radio power at 408 MHz one can infer an estimate of

the unboosted core power. The comparison between the estimated and observed core power provides constraints on the jet speed and inclination (see Giovannini et al. 2001). Using this method, for the source total flux at 408 MHz (2.38 Jy; Wright & Otrupcek 1990) and the 5 GHz core flux (∼180 mJy), we obtained a maximum inclination angle θ <30°. However, in contrast with the assumptions of the IC/CMB model, the relation implies low bulk motions, $\Gamma_{\rm bulk}$ <3, for aligned (θ <10°) jets. Indeed, we stress that these estimates should be considered indicative as this method is based on statistical samples.

As we know from other nearby examples, in particular 3C 273 (Marshall et al. 2001), the most extreme IC/CMB parameters are needed for the innermost jet knots because they have the highest X-ray to radio flux ratios (e.g. Hardcastle 2006). However, for jets with multiple knots, the IC/CMB modelling usually requires B and $\Gamma_{\rm bulk}$ decreasing with distance from the core, while, for J1512+02, the modelling indicates that significant deceleration occurs only beyond the JBF.

From the energetics standpoint, for the first two knots the X-ray$_{\rm synch.}$ model is indeed the most efficient ($L_{\rm jet} < 10^{45}$ erg s^{-1}) among the tested ones. Moreover, it is still feasible in the hypothesis of a jet that is mildly relativistic on kiloparsec scales, as supported by studies of powerful jets (see e.g. Mullin & Hardcastle 2009). X-ray synchrotron emission is observed in the kpc jets of low-power FR I radio galaxies. However, these jets differ from J1512+02 in their typical morphologies, brightest at the core and edge-dimmed, and characterized by lower X-ray luminosities. Furthermore, the X-ray photon indexes measured in FR I jets are usually >2 (see for example the case of M 87 jet, Sun et al. 2018, and references therein), while knot1 has a hard X-ray spectrum ($\Gamma_X = 1.6 \pm 0.1$). Finally, we note that this scenario is ruled out for the other two jet features, the JBF and jet termination. While we cannot exclude that different radiative and acceleration mechanisms are active along the jet, a combination of synchrotron X-ray emission for the internal components and IC emission for the external ones appears unfeasible because of the different jet parameters, in terms of kinematics and energetics, required by the models. Certainly, *HST* UV observations (as well as optical ones although more affected by contamination of the host galaxy) reaching the flux levels (∼10^{-15} erg cm^{-2} s^{-1}) of the modelled synchrotron curves should provide an effective test for this scenario.

8.2 Comparison with X-ray Jets: second synchrotron component

For a comparison of J1512+02 with other known jets, we used the sample investigated in Zhang et al. (2018), which consists of 65 knots and 29 hotspots from 41 AGN in the literature. When compared with the knots and hotspots in the sample, J1512+02 is among the most X-ray luminous jets[11] at z ≤ 0.5. This is still true when the comparison is extended to other samples, such as the jets observed by *Chandra* presented in Massaro et al. (2011): luminosities similar to those of J1512+02's components are reported for the knots of 3C 273 ($z = 0.1583$), 4C +49.22 ($z = 0.334$) and PG 1222+216 ($z = 0.432$). These sources are all core-dominated quasars with a detection in γ-rays reported in the 4FGL (Abdollahi et al. 2020). While this advocates for the importance of relativistic beaming, IC/CMB is not the only possibility. For several jets in the sample, synchrotron emission produced by a population of electrons different from those responsible for the radio emission has been proposed as an alternative explanation (Harris & Krawczynski 2002; Stawarz & Ostrowski 2002; Atoyan & Dermer 2004; Kataoka & Stawarz 2005).

In Fig. 8, the X-ray (1 keV) luminosities of the J1512+02 jet's components are plotted as a function of their radio (5 GHz) luminosities together with the sample in Zhang et al. (2018). It is evident that the radiative output of the knots in the sample is dominated by the high-energy (X-ray) component over the low-energy (radio) one (Compton-dominated SEDs). Even so, knot1 stands among those knots with the most extreme L_X/L_r ratios.

In the same range of luminosities of the knot1, with $L_X/L_r >$ 15, we find the knots of PKS 0208−512 (K0) and PKS 1136−135 (knot A). In Fig. 9, the SEDs of the knots of these two sources are compared with that of knot1. The IC/CMB mechanism is the favourite explanation for K0 of PKS 0208−512 (Perlman et al. 2011), while Cara et al. (2013) argued for a synchrotron origin of the X-ray emission of knot A in the jet of PKS 1136−135 (see also Tavecchio 2020). In both cases, optical-UV data were instrumental to conclude in favour of one or the other scenario. In PKS 0208−512, the deep upper limit at 3.69×10^{14} Hz obtained with the *HST* places hard constraints to the parameters of a putative second population of X-ray emitting particles (Perlman et al. 2011). Conversely, in PKS 1136−135 (i) the broad-band spectral shape, (ii) the high (>30 per cent) fractional polarization of the optical emission (Uchiyama et al. 2007; Cara et al. 2013) and (iii) the *Fermi* upper-limits to the jet emission in the γ-ray band (Breiding et al. 2017) can be hardly explained within the IC/CMB mechanism. A promising test case for the IC/CMB model is considered the measurement of the polarized fraction of the optical-UV flux (see Perlman et al. 2020). For highly relativistic jets, theoretical studies predict high-levels of polarization only if the CMB emission is scattered by cold electrons ($\gamma \sim 1$; Begelman & Sikora 1987), while the polarization fraction should drop to $\lesssim$8 per cent for electrons with $\gamma \gtrsim 10$ (Bonometto, Cazzola & Saggion 1970; Krawczynski 2012). For PKS 1136−135, Cara et al. (2013) estimated that the IC/CMB emission produced by cold electrons ($\gamma_{\rm min} \leq 1.2$) can reach a maximum polarization degree of ∼ 26 per cent. However, a very high bulk motion, $\Gamma_{\rm bulk} = 40$, and large beaming factor, $\delta = 20$, are needed for this contribution to be dominant in the *HST* band. In knot1 of J1512+02, the expected IC/CMB optical flux is a few 10^{-15} erg cm^{-2} s^{-1}. However, the synchrotron component responsible for the radio and sub-mm emission could be still a comparable, if not dominant, contribution in this band. Therefore, a detection at a single frequency, although accompanied by polarimetry, is not sufficient, as we need to determine the shape of the optical-UV spectrum in order to establish the origin of the optical and high-energy emission. Similar considerations also apply to knot2. In this context, optical polarimetry could be even more effective to investigate the JBF SED. In fact, the observed turnover suggests that the synchrotron radio component does not contribute beyond the ALMA band. If we extend the EED down to $\gamma_{\rm min} = 1$, the expected IC/CMB optical flux matches the tentative, g-band DECaLS detection (∼8×10^{-15} erg cm^{-2} s^{-1}). Indeed, for $\gamma_{\rm min} = 1$, the total jet power increases to 10^{47}–10^{48} erg s^{-1}. This represent certainly a critical argument for the IC/CMB model, but not a conclusive one, given the uncertainties on the jet hadronic component (as discussed in Section 8.1). Deep infrared to UV observations, reaching the flux level of the model predictions, are needed to confirm the detection, describe the shape of the spectrum in this window, and measure the polarization degree for a comparison with the theoretical expectations (see also e.g. PKS 0637−752,

[11]This statement is valid also when comparing the total X-ray emission of the jets.

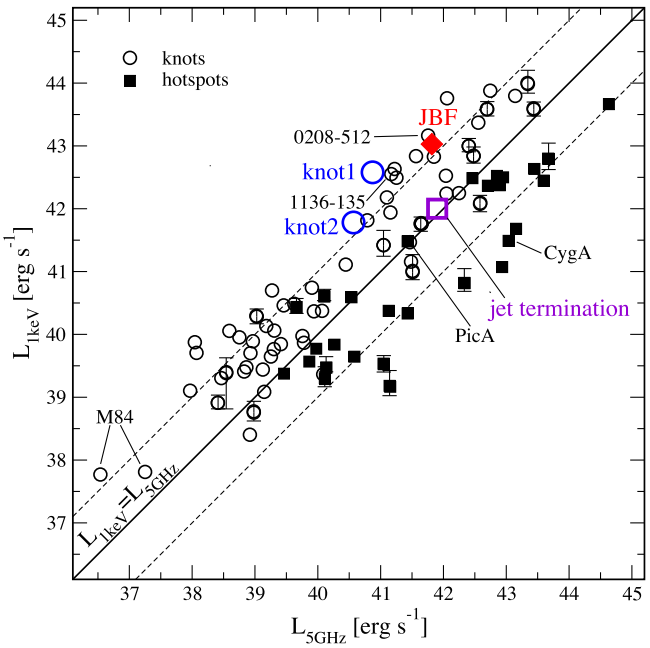

Figure 8. The 1 keV luminosity (νL_ν) of the jet features are plotted as a function of their 5 GHz luminosity together with the sample of knots (open circles) and hotspots (filled squares) presented by Zhang et al. (2018). The two X-ray detected knots of M84 jet (knot A and B in Meyer et al. 2018) are also shown. The solid line marks the equality between the two luminosities and the dashed lines correspond to $L_{1\,keV} = 0.1 \times L_{5\,GHz}$ and $L_{1\,keV} = 10 \times L_{5\,GHz}$.

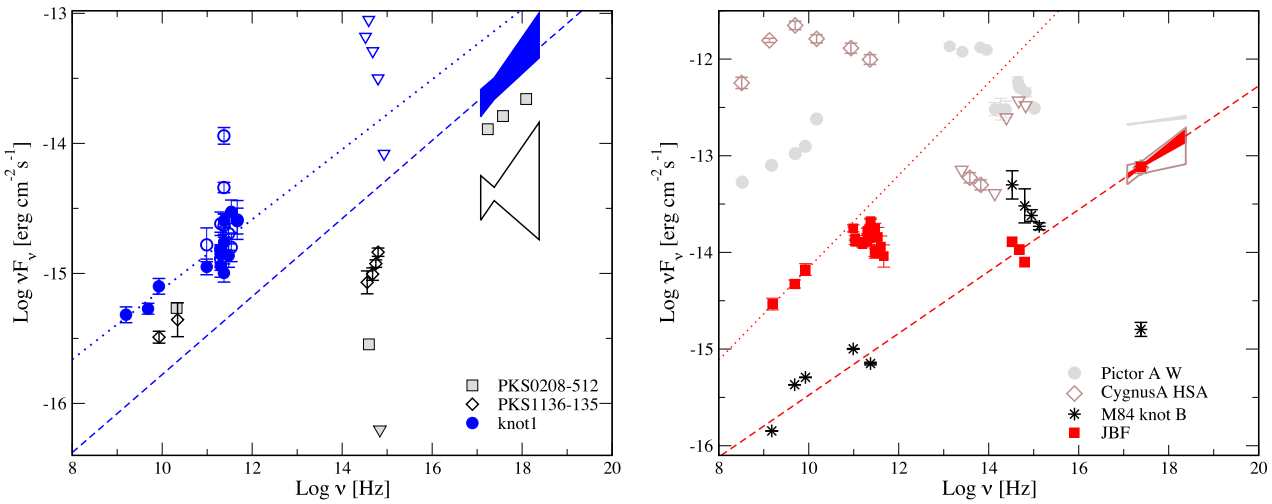

Figure 9. Left-hand panel: the radio to X-ray SED of knot1 (solid and empty blue symbols) is compared with the SEDs of the knots of two other radio quasars, PKS 0208-512 (grey squares and the triangle for the upper limit, see Perlman et al. 2011) and PKS 1136−135 (empty diamonds, see Cara et al. 2013). The dotted line and dashed lines show the slopes of the radio and X-ray spectra of knot1, respectively. Right-hand panel: radio to X-ray SED of the jet brightest feature (JBF). The tentative detection in the DECaLS images is also reported. The dotted line and dashed line represent the radio and X-ray spectral slope, respectively. The SED is compared with the SED of (i) a typical low power hotspot (Pictor A West); (ii) a typical high-power hotspot (Cygnus A); and (iii) knot B of the radio galaxy M84 (Meyer et al. 2018).

3C 273, 3C 111; Jester et al. 2007; Mehta et al. 2009; Clautice et al. 2016).

The JBF is an interesting component under multiple aspects. Its classification, either knot or a hotspot, is not immediate based on the radio properties, as discussed in Section 4, and more clues can come from the comparison with other sources. Among the hotspots in the sample of Zhang et al. (2018), only the northern hotspot of PKS 1421−490 is brighter in X-rays than J1512+02's JBF. However, PKS 1421−490's feature is also luminous in the radio band and has $L_X/L_r \sim 0.1$. The L_X/L_r of JBF is large in comparison with those of X-ray luminous hotspots in the sample of Zhang et al. (2018), which are rather in the range $L_X/L_r \sim 0.1$–1.

In Fig. 9, we compare the SED of the JBF with the SEDs of the hotspots of Cygnus A (the hotspot A) and Pictor A (the western hotspot), taken as representative of the high- and low-

power hotspots,[12] respectively. High-power hotspots, like Cygnus A, are commonly modelled with an SSC model with a-close-to-equipartition magnetic field (see e.g. Hardcastle et al. 2004; Stawarz et al. 2007; Werner et al. 2012, and references therein). In low-power hotspots, such as the western hotspot of the radio galaxy Pictor A, SSC radiation requires instead a large departure from energy equipartition, as seen in J1512+02. Once again, the alternatives appear to be either the IC/CMB model or synchrotron X-ray emission by electrons with Lorentz factors of 10^7–10^8 (e.g. Hardcastle, Croston & Kraft 2007a; Migliori et al. 2020, and references therein). The JBF is just above the divide between the two subclasses ($\sim 1.3 \times 10^{25}$ W Hz^{-1} sr^{-1} at 1.4 GHz), which however should not be considered as a strict value. The JBF SED does not resemble any of the two comparison targets. On one hand, although it also presents a low-energy synchrotron turnover above $\gtrsim$1 GHz ($\alpha_r > 0.8$; see Stawarz et al. 2007; Pyrzas, Steenbrugge & Blundell 2015; McKean et al. 2016), the SED of Cygnus A is dominated by the synchrotron component. On the other hand, the synchrotron turnover at low energies and hard X-ray spectral index of JBF make it different also from Pictor A (see Tingay et al. 2008; Hardcastle et al. 2016). To summarize, the L_X/L_r ratio and SED comparison do not favour the classification of the feature as an hotspot.

The ALMA fluxes, together with the tentative optical detection, further challenge the interpretation of the SED of JBF within standard scenarios. Detections in the mm/sub-mm band by ALMA have been reported for a number of jets (see e.g. the mini-sample in Breiding et al. 2017). However, to our knowledge, only in the inner jet of M84 has been so far observed a radio spectrum turning over at $\sim$100 GHz (Meyer et al. 2018). Intriguingly, *HST* observations of this jet unveiled a soft optical-UV spectrum. The resulting multicomponent broad-band SED cannot be easily explained in the framework of leptonic radiative models (Meyer et al. 2018). The authors argued that a viable alternative could be represented by leptohadronic processes. In the proposed scenario, the radio and optical emission would be due to synchrotron emission of electrons and protons, respectively, while X-rays would be produced by electron secondaries via synchrotron mechanism. This model implies however jet's energetics that exceed by an order of magnitude the source's Eddington limit. Indeed, the SED of knot B of M84, which we report in Fig. 9, has similarities with that of JBF, provided that in the latter the optical detection is confirmed. Although beyond the goals of our work, it could be interesting to explore the leptohadronic scenario also for J1512+02 jet. We note however that the radio and X-ray luminosities of JBF are significantly higher than those of M84 knots (in the range 10^{36}–10^{38} erg s^{-1}, see Fig. 8), and this could further enhance the issue of the jet's energy budget. Moreover, the morphologies of the two jets are also different, in that the X-ray emission of M84 does not present knotty structures.

Finally, going back to leptonic models, we note that in JBF, we do not observe any offset between the peaks of the radio and X-ray emission, as it is often observed in knots and hotspots (e.g. Harris & Krawczynski 2006). These chromatic shifts are not expected in the framework of one-zone models, as the simplest IC/CMB, while they could be a signature of particle acceleration processes taking places in multiple regions. The JBF appears wider in X-rays than in the radio band (Fig. 2), although we stress that, with the present data sets, this result cannot be considered as conclusive. On one side, this is compatible with the IC/CMB model, as the X-rays are produced by electrons with lower energies ($\gamma \approx$200–250) than those emitting in the GHz band ($\gamma \approx$ 1200–1300), which thus cool faster and diffuse on shorter distances. On the other side, such a configuration is expected also in the model proposed by Tavecchio (2020), where the X-rays are produced via synchrotron radiation by electrons accelerated in a shear layer surrounding the shock region.

In the direction orthogonal to the jet's main axis, the hard X-ray brightness profile of the JBF appears to decline faster than the soft X-ray one (Fig. 4). The peak of the emission lies on the jet's main axis. In the IC/CMB model, the radiative lifetimes of the electrons that produce the X-ray emission are $t_{\rm rad} \sim 10^5$ yr and correspond to diffusion lengths of tens of kiloparsecs. Hence, we should not observe any appreciable difference between the two X-ray bands on the scale of the profile ($\sim$3 kpc). However, this is somehow an ideal estimate as it does not account for the effects of the B field in the diffusion region, which, depending on its intensity and topology, can modify $t_{\rm rad}$ and the diffusion time-scales. On the other hand, in the synchrotron scenario, assuming $B \sim 100\,\mu$G, the X-ray emitting electrons have $\gamma \sim 10^7$ and $t_{\rm rad} \sim$80 yr, being able to diffuse over few tens of parsec at maximum (again neglecting the effects of the B field out of the acceleration site). To justify the kpc-extended region, the particle acceleration should take place in multiple compact regions or, alternatively, particles should be re-accelerated by some mechanism e.g. turbulence. In both cases, the efficiency of the process should decrease with increasing distance from the point where particles are first accelerated (such as a shock front). High-resolution polarimetric radio observations have been instrumental to probe the presence of compact regions in low-power hotspots and define their magnetic field topology (see Tingay et al. 2008; Orienti et al. 2020, respectively, for the use of very long baseline interferometry and VLA observations at 20 GHz). Similar observations could help us to resolve the structure of the JBF.

9 SUMMARY AND CONCLUSIONS

We presented an X-ray and multiwavelength study of a powerful, relativistic jet in the radio quasar RGB J1512+020A. The jet is among the brightest X-ray jets at low redshift (z<0.5) and its main features are characterized by large X-ray-to-radio luminosity ratios ($L_X/L_r \sim$1–51) in comparison with knots and hotspots of other known jets. Emission in the $\sim$97 GHz to $\sim$465 GHz band from each jet component is also visible in ALMA archival observations. For the broad-band SEDs of two jet's components, JBF and jet termination, the ALMA fluxes unveiled a turnover of the radio synchrotron spectrum at $\approx$460 GHz. Interestingly, we also report a tentative optical ($\gtrsim 2\sigma$) detection of JBF based on DECaLS images.

We investigated the origin of the high-energy emission by testing different leptonic radiative models. For all features, a synchrotron-SSC model appears disfavoured by the large ratios of the particles-to-magnetic field energy densities and the estimated kinetic powers exceeding the AGN's Eddington luminosity. In principle, a single synchrotron radio-to-X-ray component can reproduce the observed SED of the first two knots, being still compatible with the relatively shallow SDSS optical upper limits. The ALMA turnover rules out this scenario for the JBF and jet termination. As proposed for other jets, the X-ray emission can be produced via IC/CMB in a condition of quasi-equipartition, provided that the jet is still highly relativistic at kiloparsec scales ($\Gamma_{\rm bulk} \sim$17) and that it is seen at small angles ($\theta \sim 3^\circ$). However, the jet presents similarities with luminous jets of quasars such as 3C 273 and PKS 1136−135, for which a synchrotron origin of the X-ray emission from a second electron population appears favoured. Indeed this is a plausible hypothesis also for

[12]Referring to the definition in Hardcastle et al. (2004), powerful hotspots are those with 1.4 GHz luminosities $\gtrsim 10^{25}$ W Hz^{-1} sr^{-1}.

J1512+02. Theoretical work is needed to investigate the particle acceleration scenario generating (at least) two radiating electron distributions (see Borse et al. 2021; Mukherjee et al. 2021). In the SED of JBF, a confirmation of the DECaLS signal would imply either a common origin of the optical to X-ray emission (either IC/CMB or a second synchrotron curve) or, intriguingly, the presence of a third radiative component, similarly to what is observed in the jet of M84 (Meyer et al. 2018).

An important asset of this target is that the bright X-ray jet is coupled with a relatively 'quiet' core. Jets with similar luminosities are typically associated with quasar cores that are a factor $\gtrsim$50 more luminous. A bright core can overshine (part of) the extended jet or produce artefacts in the X-ray images that hinder the study of the jet (see e.g. Marshall et al. 2018). In J1512+02, the jet-to-core X-ray flux ratio is $\sim$0.26, and it makes possible to perform deep *Chandra* observations that are needed to better describe the morphology and spectrum of the bright and faint X-ray extended emission.

Observations at high-angular resolution in the radio and optical-UV bands of the total and polarized emission of the jet can probe the sites where particles are accelerated and the structure of the magnetic field (see Orienti et al. 2020; Perlman et al. 2020, and references therein). A multiwavelength approach (e.g. Werner et al. 2012; Breiding et al. 2017; Zhang et al. 2018; Migliori et al. 2020) is needed to better describe the SEDs of the emitting components, solve the degeneracies among the jet's parameters, and thus to discriminate among the different models.

ACKNOWLEDGEMENTS

The authors are grateful to ALMACAL team, in the person of Martin Zwaan', for kindly sharing the calibrated ALMA images. We thank the anonymous referee for comments that led to improve the manuscript. This project was supported by NASA grants GO7-18113X and AR4-15009X (Chandra). Part of this research was performed during GM visit to the Chandra X-ray Center (CXC) which was sponsored by the CXC Research Visitor Program. AS was supported by NASA contract NAS8-03060 to the Chandra X-ray Center. CCC was supported at NRL by NASA DPR S-15633-Y. This research has made use of data obtained from the Chandra Data Archive and the Chandra Source Catalogue, and software provided by the Chandra X-ray Center (CXC) in the application packages CIAO and SHERPA. This research has made use of SAOImage DS9, developed by the Smithsonian Astrophysical Observatory (SAO). This work has made use of the NASA/IPAC Extragalactic Database NED which is operated by the JPL, Californian Institute of Technology, under contract with the National Aeronautics and Space Administration. This research has made use of TOPCAT (Taylor 2005).

The Legacy Surveys consist of three individual and complementary projects: the Dark Energy Camera Legacy Survey (DECaLS; Proposal ID #2014B-0404; PIs: David Schlegel and Arjun Dey), the Beijing-Arizona Sky Survey (BASS; NOAO Prop. ID #2015A-0801; PIs: Zhou Xu and Xiaohui Fan), and the Mayall z-band Legacy Survey (MzLS; Prop. ID #2016A-0453; PI: Arjun Dey). DECaLS, BASS, and MzLS together include data obtained, respectively, at the Blanco telescope, Cerro Tololo Inter-American Observatory, NSF's NOIRLab; the Bok telescope, Steward Observatory, University of Arizona; and the Mayall telescope, Kitt Peak National Observatory, NOIRLab. The Legacy Surveys project is honored to be permitted to conduct astronomical research on Iolkam Du'ag (Kitt Peak), a mountain with particular significance to the Tohono O'odham Nation.

NOIRLab is operated by the Association of Universities for Research in Astronomy (AURA) under a cooperative agreement with the National Science Foundation.

This project used data obtained with the Dark Energy Camera (DECam), which was constructed by the Dark Energy Survey (DES) collaboration. Funding for the DES Projects has been provided by the U.S. Department of Energy, the U.S. National Science Foundation, the Ministry of Science and Education of Spain, the Science and Technology Facilities Council of the United Kingdom, the Higher Education Funding Council for England, the National Center for Supercomputing Applications at the University of Illinois at Urbana-Champaign, the Kavli Institute of Cosmological Physics at the University of Chicago, Center for Cosmology and Astro-Particle Physics at the Ohio State University, the Mitchell Institute for Fundamental Physics and Astronomy at Texas A&M University, Financiadora de Estudos e Projetos, Fundacao Carlos Chagas Filho de Amparo, Financiadora de Estudos e Projetos, Fundacao Carlos Chagas Filho de Amparo a Pesquisa do Estado do Rio de Janeiro, Conselho Nacional de Desenvolvimento Cientifico e Tecnologico and the Ministerio da Ciencia, Tecnologia e Inovacao, the Deutsche Forschungsgemeinschaft and the Collaborating Institutions in the Dark Energy Survey. The Collaborating Institutions are Argonne National Laboratory, the University of California at Santa Cruz, the University of Cambridge, Centro de Investigaciones Energeticas, Medioambientales y Tecnologicas-Madrid, the University of Chicago, University College London, the DES-Brazil Consortium, the University of Edinburgh, the Eidgenossische Technische Hochschule (ETH) Zurich, Fermi National Accelerator Laboratory, the University of Illinois at Urbana-Champaign, the Institut de Ciencies de l'Espai (IEEC/CSIC), the Institut de Fisica d'Altes Energies, Lawrence Berkeley National Laboratory, the Ludwig Maximilians Universitat Munchen and the associated Excellence Cluster Universe, the University of Michigan, NSF's NOIRLab, the University of Nottingham, the Ohio State University, the University of Pennsylvania, the University of Portsmouth, SLAC National Accelerator Laboratory, Stanford University, the University of Sussex, and Texas A&M University.

BASS is a key project of the Telescope Access Program (TAP), which has been funded by the National Astronomical Observatories of China, the Chinese Academy of Sciences (the Strategic Priority Research Program 'The Emergence of Cosmological Structures' Grant # XDB09000000), and the Special Fund for Astronomy from the Ministry of Finance. The BASS is also supported by the External Cooperation Program of Chinese Academy of Sciences (Grant # 114A11KYSB20160057), and Chinese National Natural Science Foundation (Grant # 11433005).

The Legacy Survey team makes use of data products from the Near-Earth Object Wide-field Infrared Survey Explorer (NEOWISE), which is a project of the Jet Propulsion Laboratory/California Institute of Technology. NEOWISE is funded by the National Aeronautics and Space Administration.

The Legacy Surveys imaging of the DESI footprint is supported by the Director, Office of Science, Office of High Energy Physics of the U.S. Department of Energy under Contract No. DE-AC02-05CH1123, by the National Energy Research Scientific Computing Center, a DOE Office of Science User Facility under the same contract; and by the U.S. National Science Foundation, Division of Astronomical Sciences under Contract No. AST-0950945 to NOAO.

Funding for SDSS-III has been provided by the Alfred P. Sloan Foundation, the Participating Institutions, the National Science

Foundation, and the U.S. Department of Energy Office of Science. The SDSS-III web site is http://www.sdss3.org/.

SDSS-III is managed by the Astrophysical Research Consortium for the Participating Institutions of the SDSS-III Collaboration including the University of Arizona, the Brazilian Participation Group, Brookhaven National Laboratory, Carnegie Mellon University, University of Florida, the French Participation Group, the German Participation Group, Harvard University, the Instituto de Astrofisica de Canarias, the Michigan State/Notre Dame/JINA Participation Group, Johns Hopkins University, Lawrence Berkeley National Laboratory, Max Planck Institute for Astrophysics, Max Planck Institute for Extraterrestrial Physics, New Mexico State University, New York University, Ohio State University, Pennsylvania State University, University of Portsmouth, Princeton University, the Spanish Participation Group, University of Tokyo, University of Utah, Vanderbilt University, University of Virginia, University of Washington, and Yale University.

DATA AVAILABILITY

All of the data underlying this article are already publicly available from NASA's HEASARC archive (https://heasarc.gsfc.nasa.gov/), *Chandra*'s Data Archive (https://cxc.harvard.edu/cda/), the NRAO archive (http://archive.nrao.edu/nvas/), the ALMA science portal (https://almascience.nrao.edu/), the SDSS-III portal (http://skyserver.sdss.org/dr13/en/home.aspx) and the website of the DESI Legacy Imaging Surveys (https://www.legacysurvey.org/).

REFERENCES

Abdo A. A. et al., 2010, ApJ, 716, 30
Abdo A. A. et al., 2010, ApJ, 720, 912
Abdollahi S. et al., 2020, ApJS, 247, 33
Aharonian F. A., 2002, MNRAS, 332, 215
Ahn C. P. et al., 2012, ApJS, 203, 21
Ajello M. et al., 2020, ApJ, 892, 105
Atoyan A., Dermer C. D., 2004, ApJ, 613, 151
Baldwin J. A., Wampler E. J., Gaskell C. M., 1989, ApJ, 338, 630
Becker R. H., White R. L., Helfand D. J., 1995, ApJ, 450, 559
Begelman M. C., Sikora M., 1987, ApJ, 322, 650
Blandford R., Meier D., Readhead A., 2019, ARA&A, 57, 467
Boccardi B. et al., 2021, A&A, 647, A67
Bonometto S., Cazzola P., Saggion A., 1970, A&A, 7, 292
Borse N., Acharya S., Vaidya B., Mukherjee D., Bodo G., Rossi P., Mignone A., 2021, A&A, 649, A150
Breiding P., Meyer E. T., Georganopoulos M., Keenan M. E., DeNigris N. S., Hewitt J., 2017, ApJ, 849, 95
Bridle A. H., Hough D. H., Lonsdale C. J., Burns J. O., Laing R. A., 1994, AJ, 108, 766
Cara M. et al., 2013, ApJ, 773, 186
Celotti A., Ghisellini G., 2008, MNRAS, 385, 283
Celotti A., Ghisellini G., Chiaberge M., 2001, MNRAS, 321, L1
Cheung C. C., Wardle J. F. C., Chen T., 2005, ApJ, 628, 104
Cheung C. C., Stawarz Ł., Siemiginowska A., 2006, ApJ, 650, 679
Cheung C. C., Stawarz Ł., Siemiginowska A., Gobeille D., Wardle J. F. C., Harris D. E., Schwartz D. A., 2012, ApJ, 756, L20
Clautice D. et al., 2016, ApJ, 826, 109
Cortes P. C. et al., 2020, ALMA Technical Handbook, ALMA Doc. 8.4, ver. 1.0. ISBN 978-3-923524-66-2
Crawford C. S., Fabian A. C., 2003, MNRAS, 339, 1163
Croston J. H. et al., 2009, MNRAS, 395, 1999
Dabhade P. et al., 2020, A&A, 635, A5
de Vries W. H., Becker R. H., White R. L., 2006, AJ, 131, 666
de Vries M. N. et al., 2018, MNRAS, 478, 4010
Dermer C. D., 1995, ApJ, 446, L63
Dey A. et al., 2019, AJ, 157, 168
Dickey J. M., Lockman F. J., 1990, ARA&A, 28, 215
Erlund M. C., Fabian A. C., Blundell K. M., Celotti A., Crawford C. S., 2006, MNRAS, 371, 29
Fabian A. C., Walker S. A., Celotti A., Ghisellini G., Mocz P., Blundell K. M., McMahon R. G., 2014, MNRAS, 442, L81
Fanaroff B. L., Riley J. M., 1974, MNRAS, 167, 31P
Fernandes C. A. C. et al., 2011, MNRAS, 411, 1909
Freeman P., Doe S., Siemiginowska A., 2001, in Starck J.-L., Murtagh F. D., eds, Proc. SPIE Conf. Ser. Vol. 4477, Astronomical Data Analysis. SPIE, Bellingham, p. 76
Fruscione A. et al., 2006, in Silva D. R., Doxsey R. E., eds, Proc. SPIE Conf. Ser. Vol. 6270, Observatory Operations: Strategies, Processes, and Systems. SPIE, Bellingham, p. 62701V
Georganopoulos M., Kazanas D., 2003, ApJ, 589, L5
Georganopoulos M., Perlman E. S., Kazanas D., McEnery J., 2006, ApJ, 653, L5
Ghisellini G., Tavecchio F., Foschini L., Ghirlanda G., Maraschi L., Celotti A., 2010, MNRAS, 402, 497
Giommi P. et al., 2012, A&A, 541, A160
Giovannini G., Feretti L., Gregorini L., Parma P., 1988, A&A, 199, 73
Giovannini G., Cotton W. D., Feretti L., Lara L., Venturi T., 2001, ApJ, 552, 508
Hardcastle M. J., 2006, MNRAS, 366, 1465
Hardcastle M. J., 2008, in Rector T., De Young D., eds, ASP Ser. Vol. 386, Extragalactic Jets: Theory and Observation from Radio to Gamma Ray. 386, p. 46
Hardcastle M. J., Harris D. E., Worrall D. M., Birkinshaw M., 2004, ApJ, 612, 729
Hardcastle M. J., Evans D. A., Croston J. H., 2007a, MNRAS, 376, 1849
Hardcastle M. J., Croston J. H., Kraft R. P., 2007b, ApJ, 669, 893
Hardcastle M. J. et al., 2016, MNRAS, 455, 3526
Harris D. E., Krawczynski H., 2002, ApJ, 565, 244.
Harris D. E., Krawczynski H., 2006, ARA&A, 44, 463.
Hewett P. C., Wild V., 2010, MNRAS, 405, 2302
Hogan B. S., Lister M. L., Kharb P., Marshall H. L., Cooper N. J., 2011, ApJ, 730, 92
Jester S., Harris D. E., Marshall H. L., Meisenheimer K., 2006, ApJ, 648, 900
Jester S., Meisenheimer K., Martel A. R., Perlman E. S., Sparks W. B., 2007, MNRAS, 380, 828
Kappes A., Perucho M., Kadler M., Burd P. R., Vega-García L., Brüggen M., 2019, A&A, 631, A49
Kataoka J., Stawarz Ł., 2005, ApJ, 622, 797
King I., 1962, AJ, 67, 471
Kraft R. P. et al., 2007, ApJ, 665, 1129
Krawczynski H., 2012, ApJ, 744, 30
Kusunose M., Takahara F., 2017, ApJ, 835, 20
Laurent-Muehleisen S. A. et al., 1997, A&AS, 122, 235
Marshall H. L. et al., 2001, ApJ, 549, L167
Marshall H. L. et al., 2010, ApJ, 714, L213
Marshall H. L. et al., 2018, ApJ, 856, 66
Massaro F., Harris D. E., Cheung C. C., 2011, ApJS, 197, 24
Massaro F. et al., 2018, ApJS, 234, 7
McKean J. P. et al., 2016, MNRAS, 463, 3143
McKeough K. et al., 2016, ApJ, 833, 123
Medvedev P. et al., 2020, MNRAS, 497, 1842
Mehta K. T., Georganopoulos M., Perlman E. S., Padgett C. A., Chartas G., 2009, ApJ, 690, 1706
Meyer E. T., Georganopoulos M., 2014, ApJ, 780, L27
Meyer E. T., Georganopoulos M., Sparks W. B., Godfrey L., Lovell J. E. J., Perlman E., 2015, ApJ, 805, 154
Meyer E. T., Petropoulou M., Georganopoulos M., Chiaberge M., Breiding P., Sparks W. B., 2018, ApJ, 860, 9
Migliori G., Orienti M., Coccato L., Brunetti G., D'Ammando F., Mack K.-H., Prieto M. A., 2020, MNRAS, 495, 1593
Mocz P., Fabian A. C., Blundell K. M., 2011, MNRAS, 413, 1107
Mukherjee D., Bodo G., Mignone A., Rossi P., Vaidya B., 2020, MNRAS, 499, 681

Mukherjee D., Bodo G., Rossi P., Mignone A., Vaidya B., 2021, MNRAS, 505, 2267
Mullin L. M., Hardcastle M. J., 2009, MNRAS, 398, 1989
O'Dea C. P., Daly R. A., Kharb P., Freeman K. A., Baum S. A., 2009, A&A, 494, 471
Orienti M., Migliori G., Brunetti G., Nagai H., D'Ammando F., Mack K.-H., Prieto M. A., 2020, MNRAS, 494, 2244
Oteo I., Zwaan M. A., Ivison R. J., Smail I., Biggs A. D., 2016, ApJ, 822, 36
Perlman E. S. et al., 2011, ApJ, 739, 65
Perlman E. S., Clautice D., Avachat S., Cara M., Sparks W. B., Georganopoulos M., Meyer E., 2020, Galaxies, 8, 71
Perucho M., Martí J.-M., Quilis V., 2019, MNRAS, 482, 3718
Petropoulou M., Vasilopoulos G., Giannios D., 2017, MNRAS, 464, 2213
Pyrzas S., Steenbrugge K. C., Blundell K. M., 2015, A&A, 574, A30
Rossi P., Bodo G., Massaglia S., Capetti A., 2020, A&A, 642, A69
Rusinek K., Sikora M., Kozieł-Wierzbowska D., Godfrey L., 2017, MNRAS, 466, 2294
Sambruna R. M., Gambill J. K., Maraschi L., Tavecchio F., Cerutti R., Cheung C. C., Urry C. M., Chartas G., 2004, ApJ, 608, 698
Sbarrato T., Ghisellini G., Maraschi L., Colpi M., 2012, MNRAS, 421, 1764
Schwartz D. A., 2002, ApJ, 569, L23
Schwartz D. A. et al., 2020, ApJ, 904, 57
Shen Y. et al., 2011, ApJS, 194, 45
Shepherd M. C., Pearson T. J., Taylor G. B., 1994, Bull. Am. Astron. Soc., 26, 987
Siebert J., Brinkmann W., Drinkwater M. J., Yuan W., Francis P. J., Peterson B. A., Webster R. L., 1998, MNRAS, 301, 261
Siemiginowska A., Smith R. K., Aldcroft T. L., Schwartz D. A., Paerels F., Petric A. O., 2003, ApJ, 598, L15.
Siemiginowska A., Stawarz Ł., Cheung C. C., Harris D. E., Sikora M., Aldcroft T. L., Bechtold J., 2007, ApJ, 657, 145
Siemiginowska A. et al., 2012, ApJ, 750, 124
Simionescu A. et al., 2016, ApJ, 816, L15
Sironi L., Spitkovsky A., 2011, ApJ, 726, 75
Spitkovsky A., 2008, ApJ, 682, L5
Stawarz Ł., Ostrowski M., 2002, ApJ, 578, 763
Stawarz Ł., Cheung C. C., Harris D. E., Ostrowski M., 2007, ApJ, 662, 213
Stocke J. T., Burns J. O., Christiansen W. A., 1985, ApJ, 299, 799
Sun X.-N., Yang R.-Z., Rieger F. M., Liu R.-Y., Aharonian F., 2018, A&A, 612, A106
Tavecchio F., 2021, MNRAS, 501, 6199
Tavecchio F., Maraschi L., Sambruna R. M., Urry C. M., 2000, ApJ, 544, L23
Taylor M. B., 2005, in Shopbell P. L., Britton M. C., Ebert R., eds, ASP Conf. Ser. Vol. 347, Astronomical Data Analysis Software and Systems XIV. Astron. Soc. Pac., San Francisco, p. 29
Tingay S. J., Lenc E., Brunetti G., Bondi M., 2008, AJ, 136, 2473
Uchiyama Y. et al., 2006, ApJ, 648, 910
Uchiyama Y. et al., 2007, ApJ, 661, 719
Ulvestad J. S., Perley R. A., Taylor G. B., eds, 2007, The Very Large Array Observational Status Summary, version August 13, 2007. Socorro, NRAO
Voges W. et al., 1999, A&A, 349, 389
Webster R. L., Francis P. J., Petersont B. A., Drinkwater M. J., Masci F. J., 1995, Nature, 375, 469
Werner M. W., Murphy D. W., Livingston J. H., Gorjian V., Jones D. L., Meier D. L., Lawrence C. R., 2012, ApJ, 759, 86
Willott C. J., Rawlings S., Blundell K. M., Lacy M., 1999, MNRAS, 309, 1017
Wills D., Wills B. J., 1976, ApJS, 31, 143
Worrall D. M., 2009, A&AR, 17, 1.
Worrall D. M., Birkinshaw M., Marshall H. L., Schwartz D. A., Siemiginowska A., Wardle J. F. C., 2020, MNRAS, 497, 988
Wright A., Otrupcek R., 1990, PKS...C, 0
York D. G. et al., 2000, AJ, 120, 1579
Zdziarski A. A., 2014, MNRAS, 445, 1321
Zhang J. et al., 2018, ApJ, 858, 27
Zhu S. F., Brandt W. N., Wu J., Garmire G. P., Miller B. P., 2019, MNRAS, 482, 2016

This paper has been typeset from a TEX/LATEX file prepared by the author.